Mon. Not. R. Astron. Soc. **000**, 1–23 (2003) Printed 21 October 2003 (MN LaTeX style file v2.2)

Searching for massive clusters in weak lensing surveys

Takashi Hamana[1,2], Masahiro Takada[3] and Naoki Yoshida[2,4]
[1] *Institut d'Astrophysique de Paris, 98bis Boulevard Arago, F 75014 Paris, France*
[2] *National Astronomical Observatory of Japan, Mitaka, Tokyo 181-8588, Japan*
[3] *Department of Physics and Astronomy, University of Pennsylvania, 209 S. 33rd Street, Philadelphia, PA 19104, USA*
[4] *Harvard-Smithsonian Center for Astrophysics, 60 Garden Street, Cambridge, MA 02138, USA*

Accepted ******; Received ******; in original form 21 October 2003

ABSTRACT
We explore the ability of weak lensing surveys to locate massive clusters. We use both an analytic model of dark matter halos and mock weak lensing surveys generated from a large cosmological N-body simulation. The analytic model describes average properties of weak lensing halos and predicts the number counts of the halos, enabling us to compute an effective survey selection function. We argue that the detectability of massive halos depends not only on the halo mass but also strongly on redshift at which the halos are located. We test the model prediction for the weak lensing peak counts against the numerical simulations, and find that the noise due to intrinsic galaxy ellipticities causes a systematic effect which increases the peak number counts. We develop a correction scheme for the systematic effect in an empirical manner, and show that, after the correction, the model prediction agrees well with the mock data. Using the mock data, we also examine the completeness and efficiency of the weak lensing halo search with fully taking into account the noise and the so-called projection effect by large-scale structures. We show that the detection threshold of S/N$=4\sim5$ gives an optimal balance between efficiency and completeness. Our results suggest that, for a weak lensing survey with a galaxy number density of $n_g = 30$ arcmin^{-2} with a mean redshift $z=1$ (which are typical of surveys with a ground based $4-10$m class telescope), the mean number of peaks is $N_{\rm peak} = 65$ per 10 square degrees for a detection threshold S/N$=4$. The contamination rate is 44%, and thus, on average, 36 out of 65 peaks (at least) are signals from real halos while the remaining 29 peaks are false peaks induced by the noise. The mean number of halos which are expected to cause lensing signals above S/N$=4$ is $N_{\rm halo}$(S/N$>4) = 37$ in the same area, whereas 23 of them are actually detected with S/N>4, giving the effective completeness as good as 63%. Weak lensing surveys thus provide a reasonably efficient way to searching for massive clusters.

Key words: cosmology: theory — gravitational lensing — galaxies: haloes — dark matter — large-scale structure of universe

1 INTRODUCTION

Recently, it has become feasible to locate massive clusters directly as density enhancements using weak gravitational lensing. Miyazaki et al. (2002) indeed discovered many clusters in a weak lensing halo survey over a 2.1 square degree field, proving the ability of weak lensing to identify massive clusters (see also Wittman et al. 2001). Unlike conventional optical or X-ray selected cluster catalogs, lensing surveys provide *well-defined* samples because the cluster selection is not biased by luminous components. This is a great advantage of gravitational lensing. However, as every other cluster survey technique (optical, X-ray and Sunyaev-Zel'dovich survey) does, lensing has its own disadvantages; for example, the projection effect from unrelated structures in the same line-of-sight. Since clusters of galaxies are one of most important cosmological probes, it is of fundamental importance to construct large homogeneous samples. Given advantages and disadvantages in each survey technique, it is desirable to combine, in a complementary manner, several techniques to construct a homogeneous catalog. Such catalogs provide a valuable data set to investigate, for example, the physical state of the intra-cluster medium. To do this, it is important to correctly understand the selection function and completeness of each survey. The primary purpose of this paper is to explore in fully detail the ability of weak lensing surveys to locate massive clusters.

It has been often argued that weak-lensing provides a truly mass-selected sample of clusters. This is not strictly true; weak lensing measures the two-dimensional tidal field which is a line-of-sight projection of the three-dimensional tidal field weighted by distance ratio ($D_l D_{ls}/D_s$, see §2 for definitions and details; see Mellier 1999; Bartelmann & Schneider 2001 for reviews of weak lensing). In simpler terms, the amplitude of the lensing signal from a cluster is not solely determined by its mass, but depends also on the redshift and the shape of the gravitational potential generated by the cluster. In addition, both foreground and background large-scale structures contribute to the lensing signal, and this projection effect usually adds a noise to the lensing signal from a halo. Further, since the weak lensing signal is measured from tiny coherent distortions in galaxy shapes, intrinsic ellipticities of galaxies introduce an irremovable noise. Thus, the detectability of weak lensing halo depends on all these factors. It is, therefore, important to carefully take these factors into account when one computes the selection function and the completeness for a weak lensing survey.

The purpose of this paper is three-fold; (1) to examine the selection function of weak lensing cluster surveys, (2) to develop the theoretical model to compute the prediction of the weak lensing halo counts, and (3) to examine the *completeness* and *efficiency* of weak lensing halo surveys under a typical observational condition from a ground based $4-10$m class telescope. To do these, we use both simple analytic descriptions of dark matter halos and mock weak lensing survey data generated from a large cosmological N-body simulation. The former offers a useful way to compute the expected lensing signals from the mass and the redshift of halos by which we compute the selection function. We also develop a theoretical model to compute the number counts of the weak lensing halos based on the analytic descriptions. On the other hand, the latter is used to examine the effects from *all* the factors mentioned above in a direct manner. The mock data is generated from lensing ray-tracing simulations combined with a dark matter halo catalog. We extensively use the mock data to explore the completeness and efficiency of the weak lensing halo search. Also the model prediction of the weak lensing halo counts is tested against the numerical simulations. We find that the model predictions agree reasonably well with the simulations.

White, Van Waerbeke, & Mackey (2002) and Padmanabhan, Seljak & Pen (2003) addressed the ability of weak lensing surveys focusing on the projection effect (see Reblinsky & Bartelmann 1999; Metzler, White & Loken 2001 for related studies on the projection effect). Our approach differs from these previous works in that we employ a more straightforward definition of the completeness. In White et al. (2002) and Padmanabhan et al. (2003), the completeness is defined as the fraction of detected halos with mass above a certain value among those that lie in the survey volume. This definition may be problematic when applied to real observations, because it mixes two completely different elements, (i) the selection effect and (ii) the effects from the individuality of the halo mass distribution, the projection and noise. We treat those two elements separately. Since the amplitude of the lensing signal depends both on the halo mass and on the redshift, halos with the same mass but located at different redshifts may or may not be detected in a survey. In order to quantify this incompleteness, we make use of the selection function to properly define "potentially detectable halos". Then we define the completeness by the fraction of the number of halos which are actually detected in the weak lensing mass map for a given detection threshold to that of halos which has an expected lensing signal (computed with the analytic descriptions of the dark matter halo) above the same detection threshold in the weak lensing survey. In other words, it measures the ratio of the number of detected halos to that of potentially detectable halos in a survey.

A major advantage of our definition and treatment is that it directly relates to observations. In making an observation strategy, one always needs to compute the expected number of detectable clusters using, for example, a simplified model, and also needs to estimate the completeness and efficiency. We use a directly observable quantity, a smoothed lensing convergence divided by the noise root-mean-square (RMS), that is the signal-to-noise ratio, S/N, of the detection, as the fundamental estimate of the lensing signal, whereas the previous studies adopted the halo mass which, under the influence of the noise and the projection effect, gives a poor estimate for the lensing signal. It is also desirable to have an accurate model to compute the expected number of halos. Our theoretical model may be useful for the weak lensing halo counts.

The rest of the paper is organized as follows. In §2, we first summarize lensing properties of massive halos predicted by the universal density profile of dark matter halos proposed by Navarro, Frenk & White (Navarro, Frenk & White 1996; 1997). Using the average properties, we compute the selection function of the weak lensing cluster survey. Next, we combine the lensing halo description with the halo mass function based on the Press-Schechter approach (Press & Schechter 1974; we adopt the modified fitting function by Sheth & Tormen 1999) to calculate theoretical predictions for weak lensing halo counts, the mass and redshift distributions. Our model, based on a simple statistical approach, should offer a theoretical basis to explore properties of weak lensing halos and also provides an optimal survey strategy. In §3, we describe our numerical experiment of weak lensing surveys and a ray-tracing technique. Statistical properties of halo catalogs are obtained and are compared with theoretical predictions derived in §2. There, we also discuss the sample variance. Using the mock weak lensing survey data, in §4, we examine the number counts of peaks in the weak lensing convergence map. The theoretical prediction developed in §2 is tested against the results from numerical simulations. In §5, we investigate the correspondence between halos and peaks identified in the lensing convergence map. In particular, we examine the completeness and efficiency of the weak lensing halo search. Specifically, we focus on the effects on the weak lensing cluster survey from the following three factors including (i) the noise due to the intrinsic ellipticities of galaxies, (ii) individualities in the matter distribution in dark matter halos, and (iii) projection effects with large-scale structures. Summary and discussion are given in §6. In Appendix A, we present some lensing convergence maps in which a missing halo or a false peak exists for illustrative examples of irregular systems. In Appendix B, we develop a correction scheme to the theoretical prediction of the weak lensing peak counts. In Appendix C, relations between the halo shape (and orientation) and the strength of lensing signal are examined.

Throughout this paper, we work with the standard flat ΛCDM cosmological model with the density parameter $\Omega_{\rm m}=0.3$, the cosmological constant $\Omega_\Lambda=0.7$, and Hubble constant $H_0=100h$km/sec/Mpc with $h=0.7$. We adopt the fitting function of the CDM power spectrum by Bardeen et al. (1986) with the normalization of $\sigma_8=0.9$. We take the observational parameters of a typical weak lensing survey from a ground based $4-10$m telescope at the present. To be specific, we consider an imaging observation with a limiting magnitude fainter than $R=25.5$ mag in a sub-arcsecond seeing condition, which provides the galaxy number density $n_g \gtrsim 30$ arcmin^{-2} with the mean redshift $z\simeq 1$.

2 PREDICTIONS FROM STANDARD MODELS

2.1 Lensing properties of an NFW halo

The universal density profile of dark matter halos proposed by Navarro, Frenk & White (1996; 1997; NFW hereafter) is given by

$$\rho_{\rm nfw}(x)=\frac{\rho_s}{x(1+x)^2}, \quad x=\frac{r}{r_s}, \tag{1}$$

where r_s is the scale radius. It is convenient to introduce the concentration parameter $c_{\rm nfw} = r_{\rm vir}/r_s$ where $r_{\rm vir}$ is the virial radius. Bullock et al. (2001) found from N-body simulations that the concentration parameter is related to halo mass as

$$c_{\rm nfw}(M, z) = \frac{c_*}{1+z}\left(\frac{M}{10^{14}h^{-1}M_\odot}\right)^{-0.13}, \tag{2}$$

where we set $c_* = 8$ for the ΛCDM model. It is important to notice that there is a relatively large scatter in this relation (Jing 2000). The mass enclosed within a sphere of radius $r_{\rm vir}$ gives the virial mass by definition:

$$M_{\rm vir} = \frac{4\pi\rho_s r_{\rm vir}^3}{c_{\rm nfw}^3}\left[\log(1+c_{\rm nfw}) - \frac{c_{\rm nfw}}{1+c_{\rm nfw}}\right]. \tag{3}$$

The virial mass is also defined by the spherical top-hat collapse model as

$$M_{\rm vir} = \frac{4\pi}{3}\delta_{\rm vir}(z)\bar\rho_0 r_{\rm vir}^3, \tag{4}$$

where $\delta_{\rm vir}$ is the threshold over-density for spherical collapse (see Nakamura & Suto 1997 and Henry 2000 for useful fitting functions). From equations (3) and (4) one can express ρ_s in terms of $\delta_{\rm vir}(z)$ and $c_{\rm nfw}$. Introducing $\delta_s = \rho_s/\bar\rho_0 - 1$, one finds,

$$\delta_s = \frac{\delta_{\rm vir}}{3}\frac{c_{\rm nfw}^3}{\log(1+c_{\rm nfw}) - c_{\rm nfw}/(1+c_{\rm nfw})}. \tag{5}$$

Although the NFW profile formally extends to the infinity, an actual halo has a finite extent. We consider a truncated NFW halo, the density profile of which is truncated at the virial radius. The surface mass density of the truncated NFW halo is given by the line-of-sight integration of the density profile (Takada & Jain 2003):

$$\Sigma(y) = \int_{-\sqrt{c_{\rm nfw}^2-y^2}}^{\sqrt{c_{\rm nfw}^2-y^2}} dz\, \rho_{\rm nfw}(\boldsymbol{y}, z) = 2\rho_s r_s f(y), \quad y = \frac{r}{r_s}, \tag{6}$$

with

$$f(y) = \begin{cases} -\frac{\sqrt{c_{\rm nfw}^2-y^2}}{(1-y^2)(1+c_{\rm nfw})} + \frac{1}{(1-y^2)^{3/2}}\operatorname{arccosh}\frac{y^2+c_{\rm nfw}}{y(1+c_{\rm nfw})}, & \text{for } y<1 \\ \frac{\sqrt{c_{\rm nfw}^2-1}}{3(1+c_{\rm nfw})}\left(1+\frac{1}{1+c_{\rm nfw}}\right), & \text{for } y=1, \\ -\frac{\sqrt{c_{\rm nfw}^2-y^2}}{(1-y^2)(1+c_{\rm nfw})} - \frac{1}{(y^2-1)^{3/2}}\arccos\frac{y^2+c_{\rm nfw}}{y(1+c_{\rm nfw})}, & \text{for } 1<y\leqslant c, \\ 0, & \text{for } y>c. \end{cases} \tag{7}$$

Note that the above expression differs from that by Bartelmann (1996) and Wright & Brainerd (2000) which is for the non-truncated NFW halo, and gives a larger surface mass density than ours. The lensing convergence profile is given by

$$\kappa(y) = \frac{\Sigma(y)}{\Sigma_{cr}} = \kappa_s f(y), \tag{8}$$

with the critical surface mass density

$$\Sigma_{cr} = \frac{c^2}{4\pi G}\frac{D_s}{D_l D_{ls}}, \tag{9}$$

and

$$\kappa_s = 3\Omega_{\rm m}\delta_s r_s\left(\frac{H_0}{c}\right)^2\frac{\chi_l(\chi_s-\chi_l)}{a(z_l)\chi_s}, \tag{10}$$

where a is the scale factor normalized at the present time, D denotes the angular diameter distance, χ denotes the comoving radial distance (which is equal to the comoving angular diameter distance for a flat universe), and the subscripts l and s stand for lens and source, respectively. It is worth noting that κ scales with $c_{\rm nfw}$ approximately as $\kappa \propto c_{\rm nfw}$ for $1 \lesssim c_{\rm nfw} \lesssim 5$ and $\kappa \propto c_{\rm nfw}^{1.5}$ for $5 \lesssim c_{\rm nfw} \lesssim 30$. It is clear that the convergence amplitude is sensitive to the halo concentration.

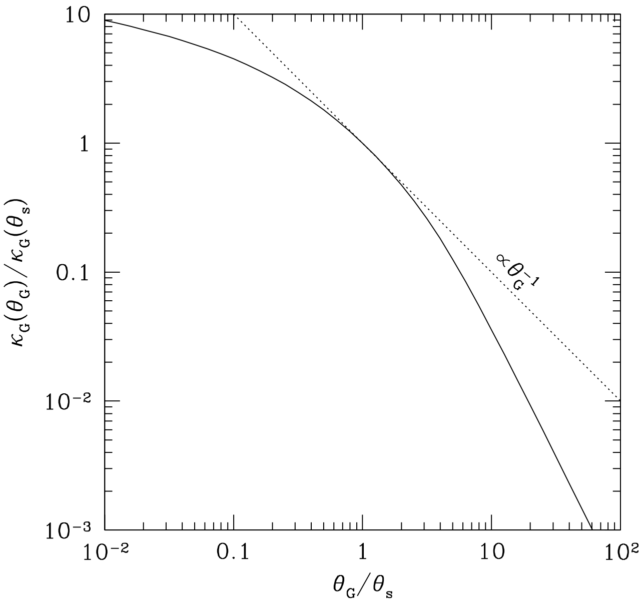

Figure 1. The solid line shows the lensing signal from an NFW halo smoothed with the Gaussian kernel (eq. (13)) against the smoothing length. For the concentration parameter, $c_{\rm nfw} = 5$ is adopted here. The dotted line shows scaling of the noise RMS with the smoothing scale ($\sigma_{\rm noise} \propto \theta_G^{-1}$, see eq. (12)).

In the presence of the noise due to intrinsic ellipticities of galaxies, a raw (un-smoothed) convergence map is very noisy. In order to have a lensing mass map with reasonably small amplitude of the noise, we smooth the convergence map with a Gaussian window function,

$$W_G(x) = \frac{1}{\pi\theta_G^2}\exp\left(-\frac{x^2}{\theta_G^2}\right). \tag{11}$$

The Gaussian smoothing is indeed adopted in real observational studies (e.g., Miyazaki et al. 2002). As shown in Van Waerbeke (2000), if intrinsic ellipticities are uncorrelated between different source galaxies, statistical properties of the resulting noise field can be described by the Gaussian random theory (Bardeen et al. 1986; Bond & Efstathiou 1987), on scales where the discreteness effect of source galaxies can be ignored. The Gaussian field is specified by the variance of the noise field that is determined by the number of galaxies contained within a smoothing aperture (Kaiser & Squires 1993; Van Waerbeke 2000):

$$\sigma_{\rm noise}^2 = \frac{\sigma_\epsilon^2}{2}\frac{1}{2\pi\theta_G^2 n_g}, \tag{12}$$

where σ_ϵ is the RMS amplitude of the intrinsic ellipticity distribution and n_g is the number density of source galaxies. Throughout this paper we adopt $\sigma_\epsilon = 0.4$ and $n_g = 30$ arcmin^{-2}, which are typical values for a survey with a limiting magnitude fainter than $R = 25.5$ mag in a sub-arcsecond seeing condition. With this choice, the noise RMS $\sigma_{\rm noise} = 0.02 \times (1\ {\rm acrmin}/\theta_G)$. It is worth noting that $\sigma_{\rm noise}$ is a direct observable in a sense that it can be esti-

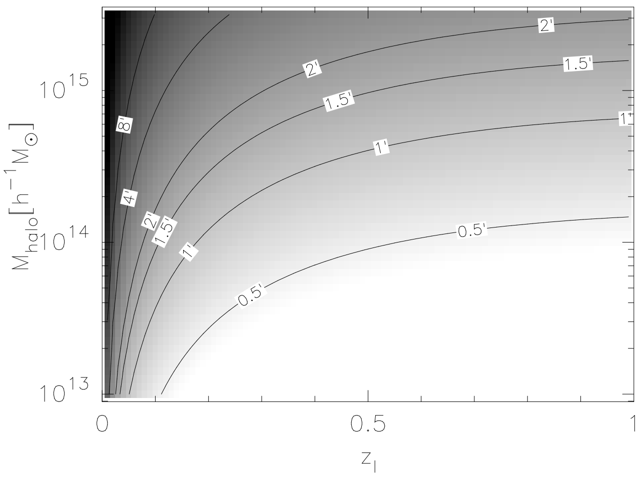

Figure 2. The gray scale with contour lines show the angular scale radius θ_s in unit of arcminutes, in the halo mass ($M_{\rm halo}$) and redshift (z_l) plane. The source redshift is fixed to be $z_s = 1$.

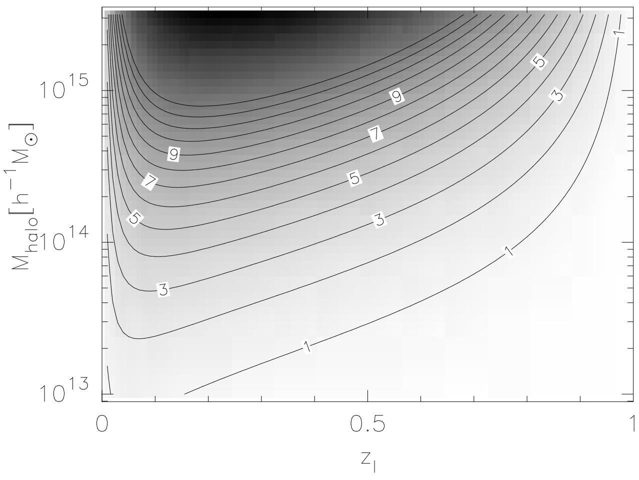

Figure 3. The gray scale with contour lines shows the S/N value for weak lensing halo detection defined by eq. (14). We adopt, throughout this paper, $\sigma_\epsilon = 0.4$, $n_g = 30{\rm arcmin}^{-1}$ and $\theta_G = 1$ arcmin.

mated from a mass reconstruction after randomizing the ellipticity direction of each source galaxy.

We need to also account for the smoothing effect on the lensing signal from a halo. The peak amplitude of the convergence profile of halos is modified by smoothing into

$$\kappa_G(\theta_G) = \int d^2\phi W_G(\phi;\theta_G)\kappa(\phi), \tag{13}$$

where the center of the smoothing kernel is set to the halo center. Hereafter we call this peak amplitude "the lensing signal due to a halo". Figure 1 plots the lensing signal as a function of the smoothing scale. The dotted line shows a scaling of the noise RMS with the smoothing scale ($\sigma_{\rm noise} \propto \theta_G^{-1}$). The comparison between the solid and dotted curves thus shows how the signal-to-noise ratio (S/N) varies with the smoothing scale. A best S/N can be attained for $\theta_G = (1-2)\times\theta_s$. Figure 2 shows the contour plot of θ_s in the halo mass and redshift plane, where the mean mass-concentration relation given by eq. (2) is adopted. Note that throughout this paper, the source redshift is fixed to be $z_s = 1$. This is a typical value for actual weak lensing survey from a ground based $4-10$m class telescope. Combination of Figures 1 and 2 suggests that $\theta_G \sim 1$ arcmin would be an optimal choice for efficient survey of massive halos with $M_{\rm halo} \gtrsim 10^{14}h^{-1}M_\odot$ at intermediate redshifts.

We define the signal-to-noise ratio, S/N, for a weak lensing halo detection by

$$\nu = \frac{\kappa_G}{\sigma_{\rm noise}}. \tag{14}$$

Figure 3 shows the contour plot of the S/N value for weak lensing halo detection in the halo mass and redshift plane. It is clear that the lensing signal from a given halo not only depends on the mass but also on the redshift, through the lensing efficiency function $D_l D_{ls}/D_s$ (see eqs. (9) and (10)). We adopt the *mean* mass-concentration relation to compute the model prediction for the S/N value, though the scatter among that relation is large (Bullock et al. 2001; Jing 2000). Since the lensing signal, κ_G, depends on the concentration parameter as $\kappa_G \propto c_{\rm nfw}^{1-1.5}$, the scatter likely translates to the scatter in κ_G value or equivalently in the S/N. It should be also noted that the lensing signal for a realistic halo is also affected by substructures and asphericity of the mass distribution, as

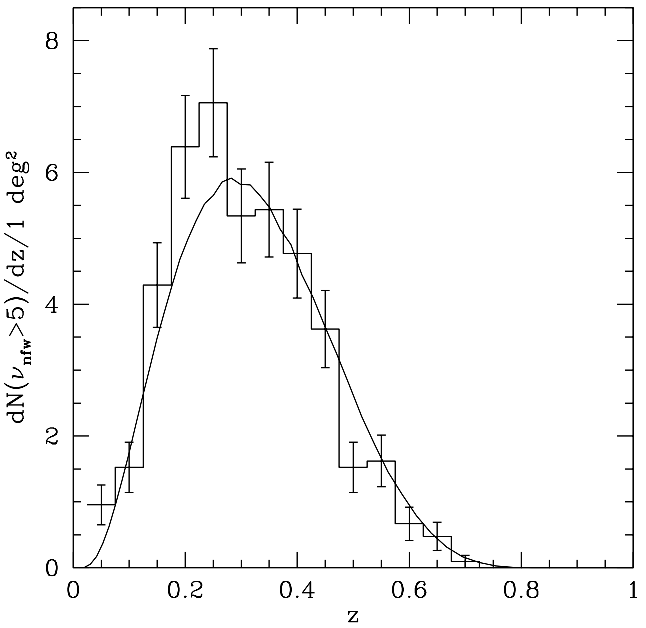

Figure 4. The redshift distribution of halos with $\nu > 5$ for the case $\theta_G = 1$ arcmin and a fixed source redshift of $z_s = 1$. The solid line shows the theoretical prediction computed using eq. (15), (see §2.2 for the detailed description). Data from mock halo catalogs of 2.048^2 square degrees are also plotted. The histogram and error bars show the mean and RMS among 50 realizations. Here the peak heights of halos in simulations are estimated from the mass and redshift, assuming the NFW profile (see §3 for details).

seen in halos of N-body simulations. We will carefully investigate these effects below, using numerical simulations.

2.2 Model prediction of weak lensing halo counts

Halos that induce a sufficiently high lensing signal are likely to be identified as peaks in the convergence map, even if the map is contaminated by the noise due to intrinsic ellipticities. Hence, it is convenient to work with the number counts of peaks above a certain threshold value: $N(>\nu;\theta_G)$. In order to compute this number

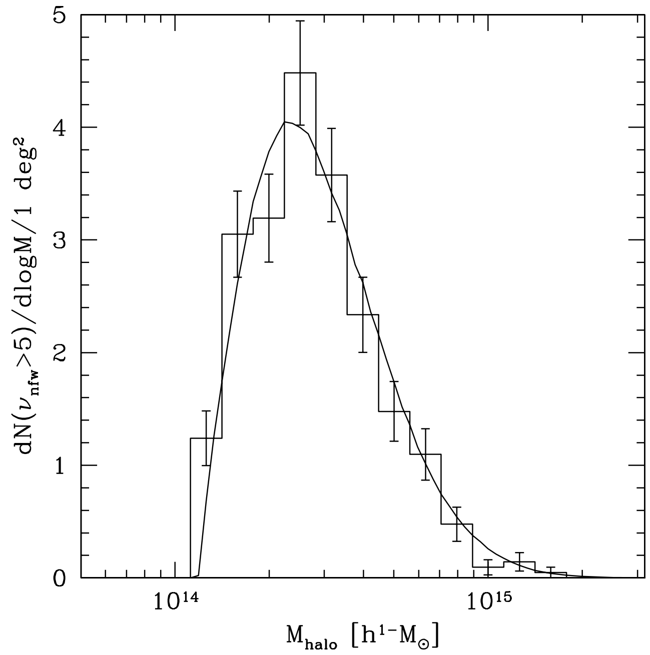

Figure 5. Mass function of halos with $\nu > 5$ for $\theta_G = 1$ arcmin and a fixed source redshift of $z_s = 1$. The solid line shows the theoretical prediction computed using eq. (15), (see §2.2 for the detailed description). The histogram and error bars show the mean and RMS among 50 realizations of mock halo catalogs of 2.048^2 square degrees (see §3 for details).

Table 1. Summary of weak lensing peak counts for various smoothing scales. The truncated NFW model is adopted computed using eq. (15). Observational parameters adopted are $\sigma_\epsilon = 0.4$, $n_g = 30\mathrm{arcmin}^{-1}$, and a fixed source redshift of $z_s = 1$. The second (third) column is for the counts $\nu > 5$ ($\nu > 4$) per 1 square degrees.

θ_G [arcmin]	$N(>5)$ [1sq. deg^{-1}]	$N(>4)$ [1sq. deg^{-1}]
0.5	1.47	3.38
1	2.08	4.05
2	1.76	3.15
3	1.30	2.27
4	0.97	1.67

counts, we assume that a high peak is generated by the lensing signal from a single massive halo and that the number of false peaks due to noise (i.e., contamination) is much smaller than that of real peaks, as will be shown below in detail. For our fiducial choice of the smoothing scale $\theta_G = 1$ arcmin, this assumption is reasonably valid for sufficiently high peaks (say $\nu > 4$), and thus we focus on such high peaks. In this case, the number density of peaks with height $\nu > \nu_{\rm th}$ per unit solid angle is given by (Kruse & Schneider 2000; Bartelmann, King & Schneider 2001)

$$N(>\nu_{\rm th};\theta_G,z_s) = \int d\chi\,\frac{dV}{d\chi}\int dM\,\frac{dn_{\rm halo}(M,z(\chi))}{dM} \times\mathcal{H}(\nu(M,z)-\nu_{\rm th}), \tag{15}$$

where χ is the radial comoving distance, $dV/d\chi$ is the comoving volume element per unit solid angle ($dV/d\chi = \chi^2$ for a flat cosmology), $dn_{\rm halo}/dM$ is the halo mass function, for which we adopt the fitting function by Sheth & Toremen (1999), and $\mathcal{H}(x)$ is the Heaviside step function ($\mathcal{H}(x) = 1$ for $x > 0$ and 0 otherwise). The differential counts are obtained by

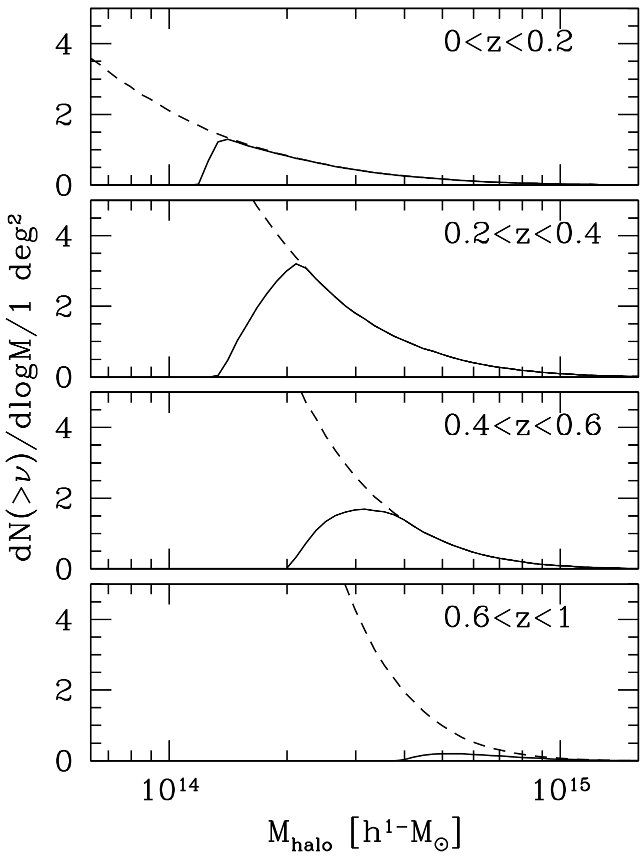

Figure 6. The solid lines show the mass function of halos with $\nu_{\rm nfw} > 5$ within a given redshift range labeled in each plot. A fixed source redshift of $z_s = 1$ is adopted. The dashed lines show the mass function of halos within the corresponding volume (which is equivalent to set $\nu > 0$, that is, no limit on the weak lensing signal is imposed).

$$\frac{dn_{\rm peak}}{d\nu} = \left|\frac{dN(>\nu;\theta_G,z_s)}{d\nu}\right|. \tag{16}$$

Table 1 summarizes the predicted weak lensing peak counts for various smoothing scales. It is shown that a choice of $\theta_G = 1$ arcmin gives the largest counts, for $\sigma_\epsilon = 0.4$ and $n_g = 30$ arcmin^{-2}. Throughout the following discussion, we adopt this smoothing scale.

Figures 4 and 5 show the redshift and mass distributions of weak lensing halos, respectively. The solid lines represent the theoretical predictions, while the histograms with error bars show the results from the mock catalogs which we describe in §3.4. The redshift distribution peaks at $z \sim 0.3$. Most of the counts comes from intermediate redshifts from $z = 0.1$ to 0.6. The lower mass limit in the weak lensing mass function shown in Figure 5 is determined by the detection threshold, while the decline in the high mass side (which has an approximate exponential slope) is due to the property of the halo mass function.

Figure 6 shows the mass distribution of halos within different redshift intervals labeled in each plot. The solid lines are for halos with $\nu_{\rm nfw} > 5$, while the dashed lines are for all the halos in the corresponding volume. The upper two plots clearly show that, up to $z = 0.4$, almost all the halos with $M > 2\times10^{14}h^{-1}M_\odot$ indeed produce high peaks with $\nu_{\rm nfw} > 5$. However, for higher redshifts, only a small fraction of massive halos produces high peaks. Thus, if a mean source redshift is around $z_s = 1$, weak lensing is not an efficient technique of finding high-redshift halos (say $z > 0.6$), except for very massive halos of $M > 5 \times 10^{14} h^{-1} M_{\odot}$. It should be noticed that the ability of the weak lensing halo surveys depends on observational conditions. In this paper, we consider a typical weak lensing survey at the present. Future, deep surveys exploiting space telescopes will be able to detect less massive halos and halos at higher redshift.

The theoretical model prediction discussed in this section provides us with a basic selection function of the weak lensing cluster survey. However, since our model is based on the simple averaged descriptions of the dark matter halos, it does not reproduce the individuality of halos which may cause a substantial scatter in the relations between the lensing signal and the mass and redshift of halos. Furthermore, there are two additional sources of scatter; the projection effect and the intrinsic ellipticity noise. In the next section, we will examine these issues in detail using numerical simulations.

3 NUMERICAL SIMULATION AND MOCK CATALOGS

3.1 N-body simulation

We used N-body data from Very Large N-body Simulation (VLS) carried out by the Virgo Consortium (Jenkins et al. 2001, and see also Yoshida et al. 2001 for simulation details). The simulation was performed using a parallel P^{3}M code (MacFarland et al. 1998) with a force softening length of $l_{\rm soft} \sim 30\, h^{-1}{\rm kpc}$. The simulation employed 512^3 CDM particles in a cubic box of $479\, h^{-1}{\rm Mpc}$ on a side. It uses a flat cosmological model with $\Omega_0 = 0.3$, $\Omega_\Lambda = 0.7$, and $h = 0.7$. The initial matter power spectrum was computed using CMBFAST (Seljak & Zaldarriaga 1996) assuming a baryonic matter density of $\Omega_{\rm b} = 0.04$. The particle mass ($m_{\rm part} = 6.86 \times 10^{10} h^{-1} M_{\odot}$) of the simulation is sufficiently small to guarantee practically no discreteness effect on dark-matter clustering on scales down to the softening length in the redshift range of interest for our purposes (Hamana, Yoshida & Suto 2002).

3.2 Weak lensing ray-tracing simulation

The multiple-lens plane ray-tracing algorithm we used is detailed in Hamana & Mellier (2001; see also Bartelmann & Schneider 1992, Jain, Seljak & White 2000 and Vale & White 2003 for the theoretical basics and technical issues); here we thus describe only aspects specific to the VLS N-body data. In order to generate the density field between $z = 0$ and $z \simeq 1$, we use a stack of 6 snapshot outputs from two runs of the N-body simulation, which differ only in the realization of the initial fluctuation field. Each cubic box is divided into 4 sub-boxes of $479^2 \times 119.75 h^{-3}{\rm Mpc}^3$ with the shorter box side being aligned with the line-of-sight direction. N-body particles in each sub-box are projected onto the plane perpendicular to the shorter box side and thus to the line-of-sight direction. In this way, the particle distribution between the observer and $z \simeq 1$ is projected onto 19 lens planes separated equally by $119.75\, h^{-1}{\rm Mpc}$. Note that in order to minimize the difference in redshift between a lens plane and an output of N-body data, only one half of the outputs (i.e. two sub-boxes) from $z = 0$ N-body box was used.

The particle distribution on each plane is converted into the surface density field on a 4096^2 regular grid using the triangular shaped cloud (TSC) assignment scheme (Hockney & Eastwood 1988). 4096^2 grid is chosen to maintain the resolution provided by the N-body simulation as well as to remove at the same time the shot noise due to discreteness in the N-body simulation. The computation follows the procedure described in Hamana & Mellier (2001) and Jain et al. (2000).

Having produced surface density fields on all lens planes, we trace 512^2 rays backwards from the observer's point using the multiple-lens plane algorithm (e.g. Schneider, Ehlers & Falco 1992). The initial ray directions are set on 512^2 grids with a grid spacing of 0.24 arcmin, and thus the total area covered by the rays is 2.048^2 square degrees. We made 50 realizations of the underlying density field by randomly shifting the simulation boxes in the direction perpendicular to the line-of-sight using the periodic boundary conditions of the simulation[1]. Note that the lens planes coming from the same box are shifted in the same way in order to maintain the clustering of matter in one box.

In the following analyses, we use the lensing convergence map of the source plane closest to $z = 1$. This is, we call, the *noise-free lensing map*.

3.3 Adding noise

To simulate a more realistic lensing survey, we add noises due to intrinsic ellipticities of source galaxies to the simulated lensing map. Actual observations are further affected by other systematics such as imperfect conditions of telescope and detector. Examining these effects is beyond the scope of the present paper, and thus we do not consider such observational effects.

As extensively shown in Van Waerbeke (2000), the noise field due to the intrinsic ellipticities is well approximated by the Gaussian random field on angular scales of our interest, if the ellipticities are uncorrelated between different sources (see also Jain & Van Waerbeke 2000). We thus model the noise field in a κ map as a random Gaussian field. The Gaussian noise added to our κ map has variance

$$\sigma_{pix}^2 = \frac{\sigma_\epsilon^2}{2} \frac{1}{n_g \theta_{pix}^2}, \tag{17}$$

where $\theta_{pix} = 0.24$ arcmin is the pixel size of our κ maps. The noise RMS on pixels is $\sigma_{pix} = 0.22$ which is much larger than the RMS of the lensing convergence field.

3.4 Halo catalogs on the light-cone

We identify dark matter halos in 5 low redshift outputs of the N-body simulation using the standard friends-of-friends algorithm with a linking parameter of $b = 0.164$ (in units of the mean particle separation). Halos with mass greater than $1 \times 10^{13} h^{-1} M_{\odot}$, which corresponds to the mass of 146 simulation particles, are used in the analyses below. We define the halo center to be the center-of-mass position of member particles.

In order to evaluate the halo shape, we compute the inertia tensor of the mass distribution;

$$\begin{aligned} I_{ij} &= \int d\boldsymbol{x}^3 (x_i - \bar{x}_i)(x_j - \bar{x}_j)\rho(\boldsymbol{x}) \\ &= m_p \sum_{k=1}^{N_p} (x_{i,k} - \bar{x}_i)(x_{j,k} - \bar{x}_j), \end{aligned} \tag{18}$$

where i, j run from 1 to 3, $\bar{x}_i$ denotes the center-of-mass position

[1] The weak lensing ray-tracing simulation data used in this paper are available from T. Hamana on request, hamanatk@cc.nao.ac.jp.

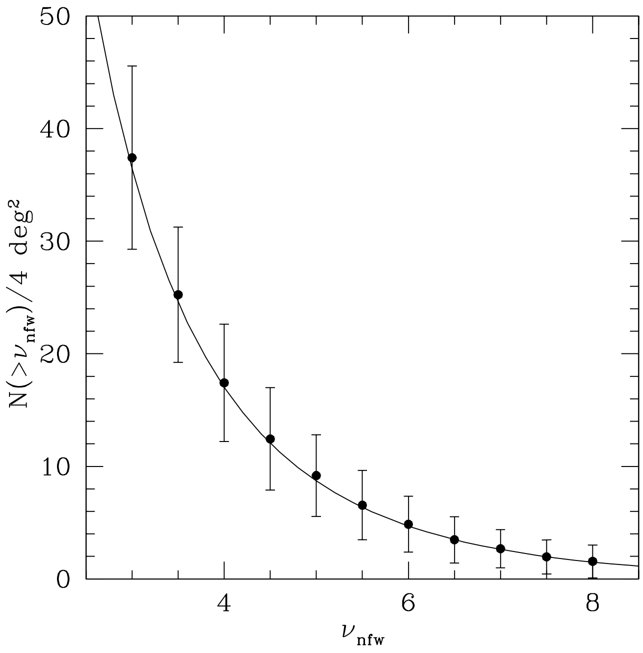

Figure 7. The number count of the lensing peaks above a given threshold $\nu_{\rm nfw}$ per a 4 square degrees area. The solid curve shows the model prediction computed from eq. (15), while the filled circles with error bars denote the simulation result as in Figure 4. Again, the peak height of a halo is estimated form the halo mass and redshift in the manner described in the text (§3.4).

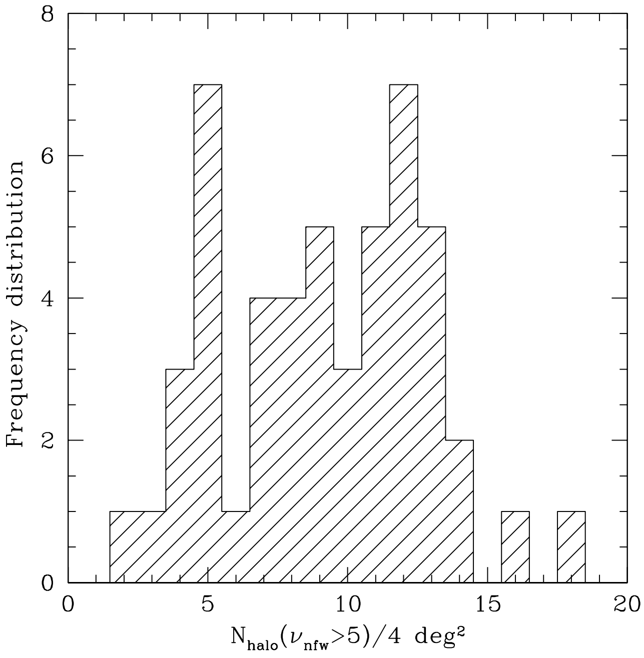

Figure 8. The frequency distribution of numbers of halos with the expected peak height (see §3.4 for its definition) $\nu_{\rm nfw} > 5$ from 50 realizations of 4 square degrees.

and N_p is the number of member particles of the halo. From the inertia tensor we compute the eigen vectors and convert them to the axial ratios a/c and a/b ($a \leqslant b \leqslant c$). We also compute the trace of the inertia tensor,

$$Q \equiv \frac{1}{3}(I_{11} + I_{22} + I_{33}). \tag{19}$$

This is compared with the expectation value for the NFW halo,

$$\begin{aligned} Q_{\rm NFW} &= \frac{4\pi}{3}\int_0^{r_{\rm vir}} dr\, r^4 \rho_{\rm nfw}(r) \\ &= M_{\rm vir} r_{\rm vir}^2 q(c_{\rm nfw}), \end{aligned} \tag{20}$$

with

$$q(c_{\rm nfw}) = \frac{c_{\rm nfw}^3 - 3c_{\rm nfw}^2 - 6c_{\rm nfw} + 6(1+c_{\rm nfw})\log(1+c_{\rm nfw})}{6c_{\rm nfw}^2[(1+c_{\rm nfw})\log(1+c_{\rm nfw}) - c_{\rm nfw}]}. \tag{21}$$

Note that $q(c_{\rm nfw})$ can be approximated by $q(c_{\rm nfw}) \simeq 0.22c_{\rm nfw}^{-0.26}$ for $3 \lesssim c_{\rm nfw} \lesssim 30$. The ratio $Q/Q_{\rm NFW}$ gives an estimate of the concentration of the mass distribution. We also define the following quantity that gives an estimate of the line-of-sight elongation of the halo mass distribution:

$$R = \frac{2I_{33}}{I_{11} + I_{22}}, \tag{22}$$

where x_3 is taken by the direction parallel to the line-of-sight. This is rather a crude estimation, generally, halos elongated along or perpendicular to the line-of-sight have $R > 1$ or $R < 1$.

Halo catalogs on the light-cone are generated stacking the simulation outputs in the same manner as in the ray-tracing simulation. We use the 50 realizations which have the same underlying matter distribution as used in the weak lensing data. This combined data set allows us to directly relate the distribution of dark matter halos to the weak lensing convergence map.

In summary, each halo in the mock catalogs has data on the mass, the estimates of the halo shape Q and R defined by eqs. (19) and (22), respectively, the redshift computed from the radial distance to a halo, and the angular position converted from the spatial positions. In addition, for each halo, we compute the virial radius and the concentration parameter using eqs. (4) and (2), from the halo mass and redshift of N-body data output time (which are $z = 0$, 0.1, 0.3, 0.5 and 0.8). These values allow us to estimate the *expected* lensing signal using eq. (13) with eq. (8) which is the expected lensing signal if the halo has the NFW profile. Similarly, we also compute $Q_{\rm NFW}$ using eq. (20). Moreover, we introduce a $flag$ parameter for each halo, to quantify the following possible problem that arises from our use of multiple-lens plane ray-tracing algorithm. As a result of projection of N-body particles into 4 lens planes, member particles of given one halo located close to the boundary could be separated into different planes. Thus, such a split halo would generate an artificially deformed (or even separated) lensing signal in a κ map. We assign $flag = 1$ for such halos whose virial radius is larger than the distance between the halo center and the closest plane, $flag = 2$ for halos whose scale radius is larger than the distance to the closest plan, and $flag = 0$ otherwise. The fraction of flagged halos is very small, 0.88% for $flag = 1$ and 0.19% for $flag = 2$, thus it does not have significant influence on our analyses below, but we carefully check if flagged halos cause any artificial eccentric signals in the lensing convergence map.

The *expected* lensing signal of each halo is converted into the peak height in the same way as eq. (14), which we denote as $\nu_{\rm nfw}$. Total numbers of halos with $\nu_{\rm nfw} > 5$ and $\nu_{\rm nfw} > 4$ in our 50 realizations are 459 and 871, respectively, which are sufficiently large to allow the statistical analyses of weak lensing halos.

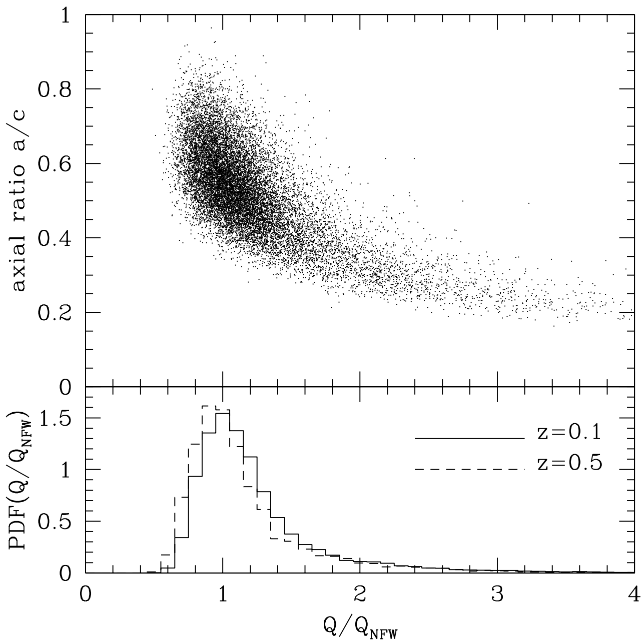

Figure 9. *Upper panel*: the scatter plot showing the relation between $Q/Q_{\rm NFW}$ and the axial ratio a/c for halos with $M > 3 \times 10^{13}h^{-1}M_\odot$ in the $z = 0.1$ output. Here $Q_{\rm NFW}$ is defined by eq. (20) and is computed using the relation eq. (4). *Lower panel*: the PDF of $Q/Q_{\rm NFW}$ of halos with $M > 3 \times 10^{13}h^{-1}M_\odot$, the solid and dashed lines for $z = 0.1$ and $z = 0.5$ outputs, respectively.

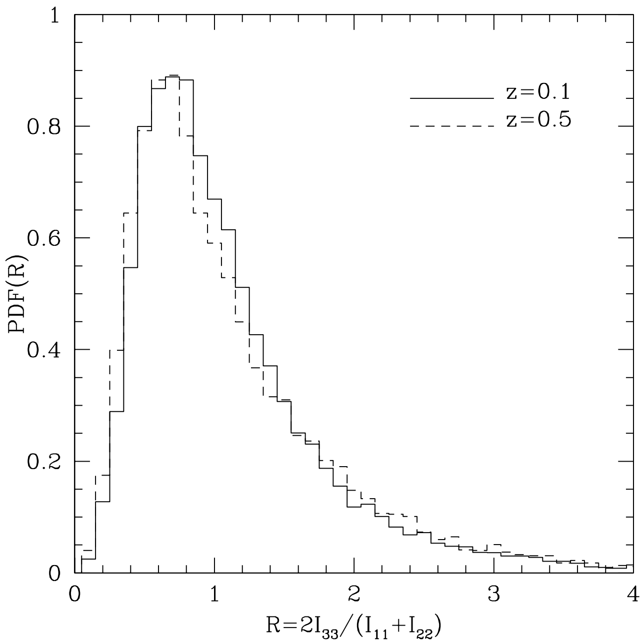

Figure 10. The PDF of the R defined by eq. (22) for halos with $M > 3\times10^{13}h^{-1}M_\odot$ at $z = 0.1$ (solid line) and $z = 0.5$ (dashed line) outputs. Note that the median of the distributions is ~ 0.92, and 55% of the all samples has $R < 1$.

Figure 7 plots the accumulate number counts of halos against the *expected* peak height, $\nu_{\rm nfw}$. The solid curve is the theoretical prediction of eq. (15) and well matches the simulation result. This agreement is not surprising, because ingredients of the theoretical model (the universal profile and halo mass function) are calibrated by N-body simulations.

The counts of halos with $\nu_{\rm nfw} > 5$ in 2.048^2 square degrees is found to be $N(\nu_{\rm nfw} > 5) = 9.18 \pm 3.63$, where the error represents the RMS among 50 realizations. This is in good agreement with the theoretical prediction of 8.71. However, the RMS is somewhat large and slightly larger than the Poisson fluctuation. Figure 8 shows the distribution of numbers of halos with $\nu_{\rm nfw} > 5$ in each realization, quite a wide spread is evidently seen. This is mainly due to the very strong clustering of massive halos. Accordingly, given a limited survey area, the halo counts significantly varies from survey to survey.

The lower panel of Figure 9 shows the PDFs of $Q/Q_{\rm NFW}$ computed from massive halos with $M > 3 \times 10^{13}h^{-1}M_\odot$ ($Q_{\rm NFW}$ is computed using the mean mass–concentration relation eq. (2)). The PDF peaks at $Q/Q_{\rm NFW} \sim 1$ as expected, but has rather broad distribution. No significant difference in the PDFs between the five different redshift boxes is observed. The upper panel shows the scatter plot in $Q/Q_{\rm NFW}$–a/c plane for halos with $M > 3 \times 10^{13}h^{-1}M_\odot$ from $z = 0.1$ output. It is evidently seen in the plot that the mass concentration defined by $Q/Q_{\rm NFW}$ correlates with the axial ratio, which implies that an extended mass distribution is likely associated with eccentric mass distributions such as halos having substructures or on-going merger. We note that the PDF of axial ratio peaks at $a/c \sim 0.5$ and thus most of halos significantly deviate from the spherical symmetry. This broad distribution leads to significant scatter in the relation between the expected and observed lensing signals as seen below.

Figure 10 shows the PDF of the shape parameter R defined by eq. (22) for massive halos with $M > 3\times10^{13}h^{-1}M_\odot$. A broad distribution is evidently seen and we checked that the distribution does not largely change over the redshift range we considered ($z < 0.8$). It is important to note that the median of the distribution is less than unity (~ 0.92), thus more than half of the massive halos (specifically 55% for halos with $M > 3\times10^{13}h^{-1}M_\odot$, irrespective of the redshift) have $R < 1$. This is a natural consequence of the random orientation of the halos' major axis; since among the spatial three directions, one is the line-of-sight direction and the others are perpendicular to it, there is higher probability that the major axis of a halo is elongated along either of two directions perpendicular to the line-of-sight rather than along it. The skewed distribution leads to systematic bias in the relation between the expected and observed lensing signals (see §5.2 and Appendix C for details).

3.5 Visual impressions

Figure 11 represents the lensing convergence map taken from one of the 50 realizations. The color scale shows κ value on the 512^2 pixels with the pixel size of 0.24 arcmin. Figure 12 shows the same convergence map as in Figure 11 but after smoothed by the Gaussian filter function of $\theta_G = 1$ arcmin. Adding the Gaussian noise yields the noisy map shown in Figure 13. While the noise indeed alters the appearance of the convergence map, the very high peaks remain identifiable.

Figure 14 shows the distribution of all the halos identified by the FOF scheme in the original N-body simulations, in the convergence map in Figure 11-13. Note that the size of point scales with halo masses. A good correspondence in positions between massive halos and high lensing signals on the κ map is seen. This correspondence is more clearly seen if halos are selected by means of the expected $\nu_{\rm nfw}$ value: In Figure 11, the positions of halos with $\nu_{\rm nfw} > 4$ are overlaid on the κ-map, where the plus and circle

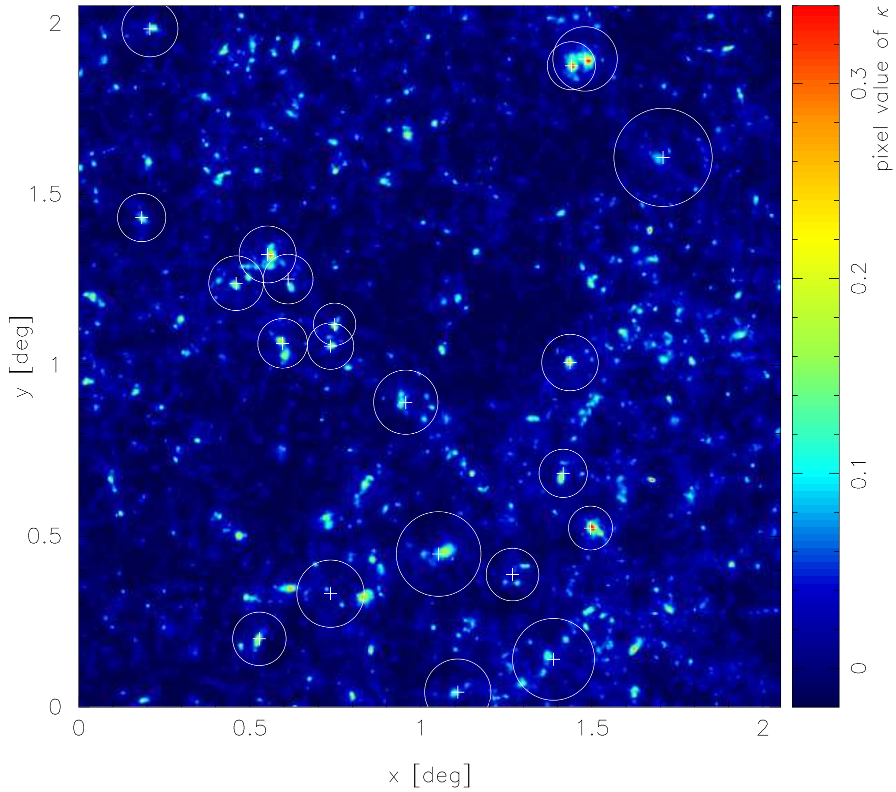

Figure 11. The color scale shows one ray-tracing realization of the lensing convergence map on the 512^2 pixels with the pixel size of 0.24 arcmin. The cross symbols show the positions of halos with $\nu_{\rm nfw} > 4$, while the circle around each halo shows the projected virial radius (see §. 3.4 for details).

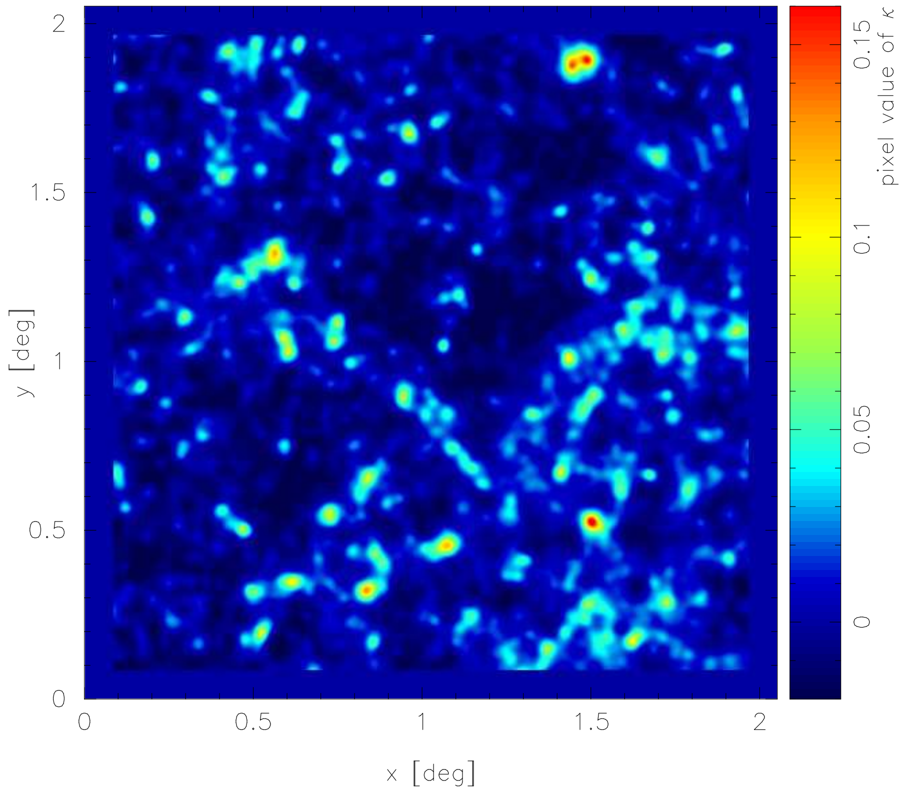

Figure 12. Same as Figure 11 but the convergence map is smoothed by the Gaussian window function with $\theta_G = 1$ arcmin. The edge regions of the field with 5 arcmin width are masked because of incomplete smoothing due to the lack of κ data on outer region.

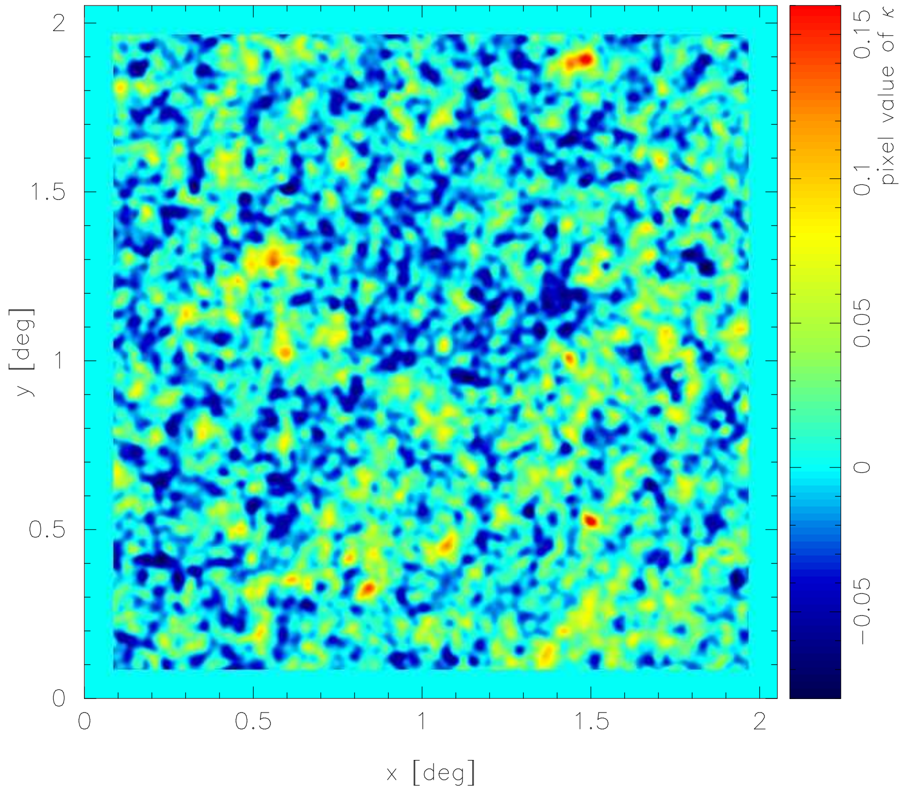

Figure 13. Same as Figure 12 but the Gaussian noise is added before smoothing is applied. From comparison with the previous figure, it is clear that high peaks due to massive halos are still identifiable.

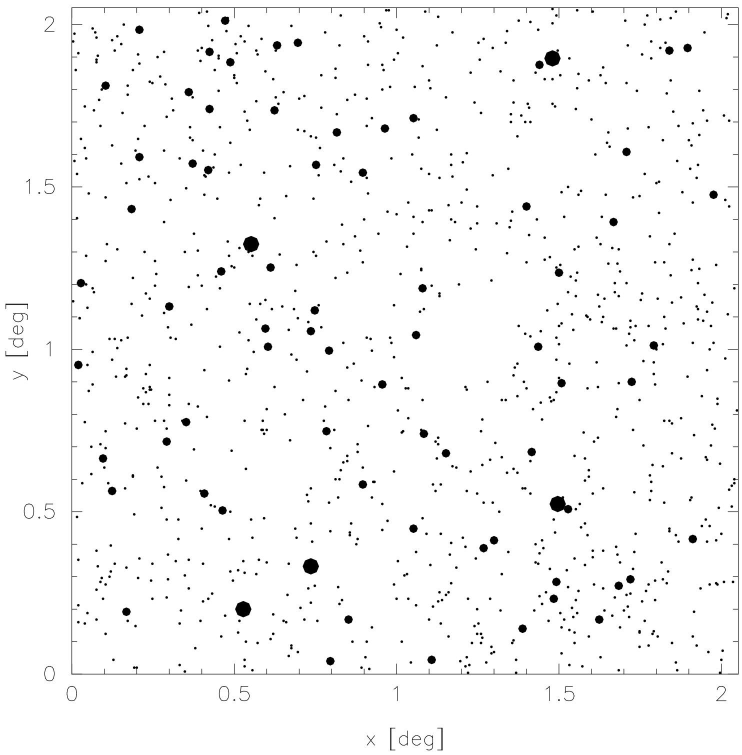

Figure 14. The celestial distribution of halos identified from N-body data using the friends-of-friends algorithm (see §3.4 for details). The underlying mass distribution on the light-cone is same as that of Figure 11. The large filled circles denote halos with $M_{\rm halo}[h^{-1}M_\odot] > 3\times10^{14}$, the small filled circles are for $3\times10^{14} > M_{\rm halo}[h^{-1}M_\odot] > 8\times10^{13}$ and the dots are for $8\times10^{13} > M_{\rm halo}[h^{-1}M_\odot] > 1\times10^{13}$. Only the halos within redshift interval between 0.1 and 0.7 are displayed.

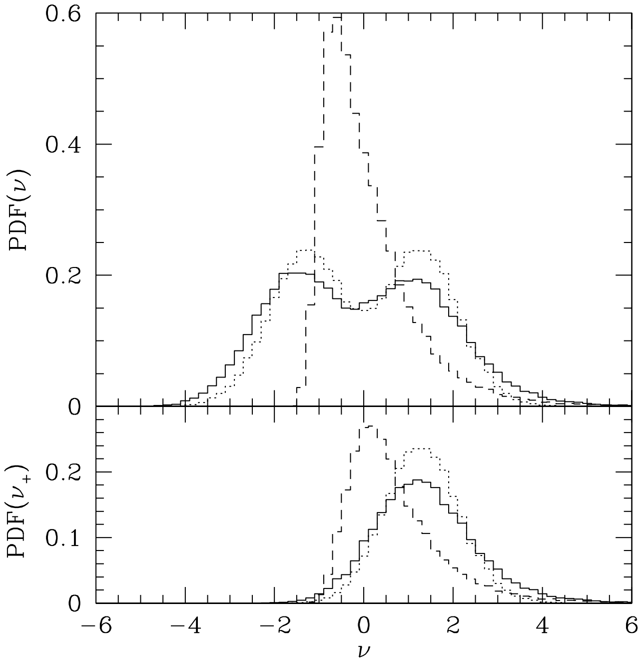

Figure 15. The simulation results for the PDFs of the peaks in the noise-free κ (dashed histogram), in the noisy κ map (solid histogram) and in the pure noise map (dotted histogram). Shown is the cumulative results from the 50 realizations. The upper panel shows the sum of the positive and negative curvature peaks, while the lower panel shows the contribution from the positive peaks only. In the total 50×2.048^2 square degrees area, there are 59,908, 107,165 and 114,250 peaks for the noise-free κ, the noisy κ map and the pure noise map, respectively. The corresponding numbers for positive curvature peaks are 31,043, 107,165, and 57,141.

show the halo center and the angular virial radius, respectively (see §3.4). The improvement in the correspondence reflects the fact that the lensing signal is determined by combined contributions of the halo mass, the redshift and the halo concentration, rather by the mass alone.

4 RESULTS ON PEAK COUNTS

In this section, we study the number counts of high peaks in the lensing convergence map. To do this, we use three kinds of κ maps; (i) the noise-free κ maps, (ii) the noisy κ maps where the Gaussian noise was added in the manner described in §3.3, and (iii) the pure noise maps without the cosmological κ signals. All these maps are smoothed with a Gaussian window function with $\theta_G = 1$ arcmin (eq. [11]). We identify positive (negative) peaks in the maps as pixels that have higher (lower) values of κ than all the eight surrounding pixels (Jain & Van Waerbeke 2000, and also see Miyazaki et al 2002 for the first application to actual observational data). The peak height is defined as the ratio of the convergence value at the peak to the noise RMS, as given by eq. (14). For all the three cases, $\sigma_{\rm noise} = 0.02$ ($\sigma_\epsilon = 0.4$ and $n_g = 30 \mathrm{arcmin}^{-2}$) are adopted.

4.1 The peak PDF

The probability distribution function (PDF) of peaks in the convergence map is studied in detail by Jain & Van Waerbeke (2000). Here we briefly summarize the characteristics of the peak PDF that are relevant for the subsequent discussion.

Figure 15 shows the peak PDFs in the noise-free κ (dashed histogram), the noisy κ map (solid histogram) and the pure noise map (dotted histogram). The upper panel shows the sum of the positive and negative curvature peaks, while the lower panel shows the contribution from the positive peaks only. In the absence of the noise, the peak PDF reflects the characteristics of the nonlinear gravitational clustering. Most of negative peaks are due to the negative curvature peaks. There is a cutoff in the negative peak height because the mass density contrast cannot be lower than -1. One can also find a tail toward the high positive peak height which arises from the lensing signals due to massive halos. Another noticeable feature seen from the lower panel is that some of the *positive* curvature peaks have a *negative* peak height, which occurs when the peak due to a halo is superposed on a void region in the same line-of-sight. If the noise field is Gaussian, the PDF from the pure-noise map is derivable from the the Gaussian random theory (Bardeen et al. 1986; Bond & Efstathiou 1987; Van Waerbeke 2000). The symmetric bimodal feature of the peak PDF is due to the superposition of two contributions from peaks with positive and negative curvatures. While adding the noise to the cosmological κ map alters the peak PDF drastically, there remain some characteristic features that contain useful cosmological information. First, the asymmetric double peaks are due to the skewed feature of the cosmological κ PDF as stated above. Second, there are excesses over the noise PDF on both high positive ($\nu > 3$) and negative peaks ($\nu < -3$). These features were indeed detected in the recent weak lensing survey by Miyazaki et al. (2002).

It is worth pointing out that the pure noise PDF can be directly estimated from an actual observed data. First, we can generate a pure noise field by mass-reconstruction after randomizing the orientation of source galaxy images (to remove coherent image distortions from lensing signals), and then we can measure the peak PDF in the pure noise map, as was performed in Miyazaki et al. (2002). This allows one to estimate the contamination rate (the false peak rate) directly from the data.

4.2 High peak counts

In the following, we restrict our discussion to the number counts of high peaks that are mainly due to massive halos. Figure 16 shows the number density of (positive curvature) peaks per 1 square degrees. The histograms show the average values computed from the 50 realizations of the numerical simulations; the noisy κ maps (solid), the noise-free κ maps (dashed) and pure the noise realizations (dotted). The long-dashed line shows the model prediction from eq. (16), while the dot-dashed line shows the prediction for the pure noise count based on the Gaussian random field theory (e.g., Bond & Efstathiou 1987; Van Waerbeke 2000). From comparison between the results for the lensing maps with and without the noise, it is clear that the noise significantly increases the peak counts over a range of peak heights we have considered. Even high peaks with $\nu > 5$ are similarly boosted, while there is no such event in the pure noise counts, as shown by the dotted curve. There are two main reasons for the the enhancement (see Appendix B for further details). First, addition of the noise leads to modifications of the peak height as well as of the peak position. Second, the noise generates spurious peaks in the noisy maps. In particular, the latter effect is likely to show up in a biased way depending on the peak height. Since the convergence field around a given high peak has greater amplitude than the average field, adding the noise onto such a region is more likely to induce spurious high peaks around the real peak. We develop a correction scheme to the model

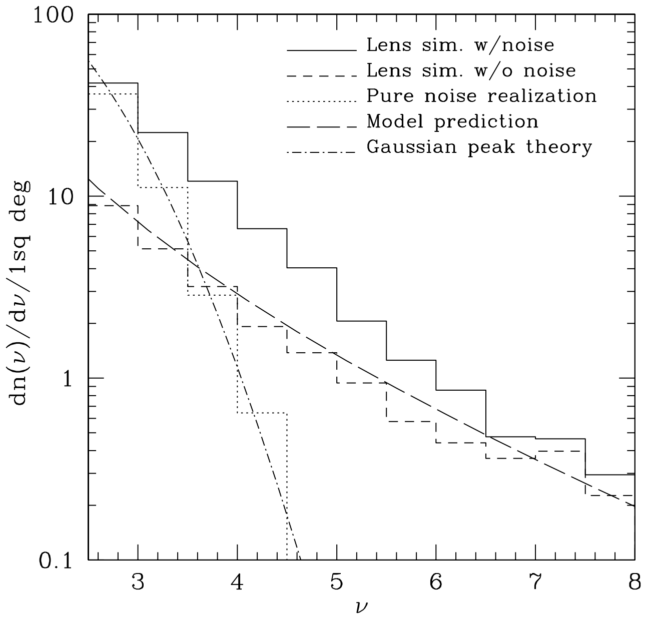

Figure 16. Counts of peaks per 1 square degrees. The histograms are from numerical experiments; the noisy κ maps (solid), the noise-free κ maps (dashed) and the pure noise realizations (dotted). The long-dashed line shows the model prediction, eq. (16) with eq. (15) and the dot-dashed line shows the prediction by Gaussian random field theory (e.g., Bond & Efstathiou 1987; Van Waerbeke 2000).

peak counts in Appendix B. The corrected counts are in reasonable agreement with the simulation result for high peaks $\nu > 5$.

5 RESULTS ON THE CORRESPONDENCE BETWEEN HALOS AND PEAKS

In this section, we examine correspondences between massive halos and peaks in the weak lensing convergence maps, using the results of our ray-tracing simulation and the halo catalogs created from the N-body simulation outputs. In doing so, we follow a realistic procedure which is to be used in weak lensing surveys: we focus on high peaks above a certain threshold in the lensing map as strong candidates for halos. The usefulness of the weak lensing halo search can be quantified in terms of *completeness* and *efficiency*. Here, completeness represents the fraction of massive halos identified as high peaks in the lensing maps, while efficiency is the fraction of high peaks that correspond to real halos. As will be shown later in detail, choosing a threshold $\nu_{th} = 4 \sim 5$ gives an optimal balance between the efficiency and completeness. We will also carefully examine if there is a correlation between the detectability of halos and their shape, which may potentially produce a bias in halo catalogs constructed from the weak lensing method.

In order to make realistic weak lensing survey catalogs, we impose a criterion on the field selection of simulations so that no nearby massive halo is included in the target fields. Specifically, we discard simulated fields if there is a halo (or possibly more) with $M_{\rm halo} > 10^{14}h^{-1}M_{\odot}$ at $z < 0.1$. Similar criterion, such as no known nearby X-ray luminous cluster of galaxies or no nearby optically identified massive cluster, are usually imposed on the field selection of an actual observation, because such a nearby massive cluster occupies a large portion of a survey field and makes a distant halo search difficult and inefficient. With this criterion, 31 fields

Table 2. Classification of matching relations between halos and peaks. The double-lined arrows denote the primary match, while the single-lined arrows denote the secondary match. The last two columns summarize the number of halos/peaks in each class, the third (fourth) column is for matching between the halo catalog and the peak list from the noise-free (noisy) κ map. Note that halos with $\nu_{\rm nfw} > 3$ (856 halos in total) and peaks with $\nu_{\rm lens} > 3$ (669 peaks) and $\nu_{\rm noisy} > 3$ (2417 peaks) are considered.

class	matching relation	number of objects	
		$\nu_{\rm nfw}$-$\nu_{\rm lens}$	$\nu_{\rm nfw}$-$\nu_{\rm noisy}$
i	halo $\underset{\Leftarrow}{\Rightarrow}$ peak	475	624
ii	halo with no paired peak	367	222
iii	peak with no paired halo	177	1637
iv	halo $\underset{\leftarrow}{\Rightarrow}$ peak	14	10
v	halo $\underset{\Leftarrow}{\rightarrow}$ peak	17	156

out of the 50 simulated fields are retained. In addition, we discard one field in which there is a massive halo with $\nu_{\rm nfw} > 5$ having $flag = 2$ (see §3.4 for a description of $flag$ [2]). We analyze the remaining 30 fields. We note that we do not use data in edge of each simulated field that has a width of 5 arcmin because of the incomplete smoothing due to the lack of data at the outer region. The total field size is then 106 square degrees.

5.1 Matching halos with peaks in lensing mass maps

We shall now examine how often massive halos indeed induce high peaks in the weak-lensing maps. As discussed in §3.4, using the halo catalogs we can compute the expected peak height $\nu_{\rm nfw}$ for each halo from the mass and redshift. We restrict our discussion to halos with $\nu_{\rm nfw} > 3$ only. The halo catalogs contain 856 such halos in total. On the other hands, the ray-tracing simulations directly enable us to find peaks in the κ maps. We consider two kinds of the κ maps; those with and without the noise due to the intrinsic ellipticities. The peaks in the two maps are identified in the manner described in §4. The noise-free maps contain 669 peaks with $\nu_{\rm lens} > 3$, while the noisy maps contain 2417 peaks with $\nu_{\rm noisy} > 3$. Clearly, the noise enhances the peak counts. It is also worth noting that the 669 peaks in the noise-free maps is significantly smaller than the *expected* number of peaks from the halo catalogs. We will carefully investigate this discrepancy in the subsequent sections.

We consider halos and peaks with $\nu > 3$ only in order to avoid associating peaks with physically unrelated halos. Because of a large number density of low mass halos, including such halos rapidly increases the chance of this mis-matching. This is especially the case when one attempts to match peaks in noisy κ maps with halos because false peaks due to the noise can be accidentally matched with physically unrelated halos. The value $\nu > 3$ is chosen based on the fact that such high peaks are expected to be caused by real halos, even when the lensing map is contaminated by the noise (see Figure 16). Also the value is reasonably smaller than the observational threshold value which is generally set by $\nu \gtrsim 4$.

We carry out the peak-halo matching in two directions by checking whether a peak has a corresponding halo in the halo catalog, and whether a halo has a counter-peak in the simulated κ map. Note that the peak position does not necessarily agree with

[2] Including this field in our analysis below does not change the conclusions, but we decided to discard it for having conclusive results.

the center-of-mass position (which is defined as the position of the halo) and this is more likely the case for halos that have substructures or are in the merger process. For this reason, we search for a matched pair candidate within a radius of 12 pixels (2.88 arcmin) from the peak position or from the halo center. This maximum angular separation 2.88 arcmin is chosen so that it is larger than the smoothing radius of $\theta_G = 1$ arcmin, while it is still smaller than the angular virial radius of a massive halo. If there are more than one pair candidate within the radius, we take the closest one as the primary candidate and consider the other as the secondary candidate.

We classify the peak-halo matching into the following five classes: Class-(i) is that the both directions agree; both a halo and a peak are their primary pair candidates. Class-(ii) is defined as halos that have no paired peak within a radius of 12 pixels from the halo center. We will call such halos as *missing halos*. Class-(iii) is defined as peaks with no paired halo within a radius of 12 pixels from the peak position. We will often refer to such peaks as *false peaks*. Class-(iv) denotes a halo that has a matched peak candidate, but is not the primary matched halo of that peak. Class-(v), which is the opposite to the class-(iv), is that a peak has a matched halo candidate but is not the primary matched peak of that halo. The results for the noise-free and noisy maps are summarized in Table 2.

Typical properties of halos or peaks in the class-(ii-v) are explained as follows. The class-(ii) halos are those which have a lower peak height than the threshold value ($\nu = 3$) though the expected peak heights, $\nu_{\rm nfw}$, exceed the threshold. This is mainly due to departures from the NFW profile or/and the projection effect. In the class-(iii) peaks there are two kinds: The first is that peaks which have corresponding halos but their expected peak heights, $\nu_{\rm nfw}$, are lower than the threshold value, though the measured peak heights in a κ map exceed the threshold. This is again due to departures from the NFW profile or/and the projection effect. The other is that peaks which do not have corresponding halos but are generated by the noise. The former accounts for most of the class-(iii) peaks in noise-free κ maps, while the latter accounts for a large fraction of them in noisy κ maps. The class-(iv) halos are due to the projection effect; if two or more halos are located at different redshifts along almost the same line-of-sight, after smoothing of the $kappa$ map only one peak appears, because the smoothing merges those into one structure. Finally, in the class-(v) peaks there are two kinds: The first is peaks due to substructures within a halo. This accounts for most of the class-(v) peaks in noise-free κ maps. The other is false peaks due to the noise generated around the primary peak due the massive halo. Because the convergence field around the halo peak is biased and thus larger than the average field, and adding the noise into the region is more likely to generate false peaks with a relatively high peak height. This accounts for most of the class-(v) peaks in noisy κ maps.

In the rest of this section, we consider the class-(i-iii) objects only, and do not deal with the class-(iv) and (v) objects because the class-(iv) and (v) objects are the secondary matched pairs associated with the primary matched pair in the vicinity. This roughly mimics the actual observation procedure, in which the secondary objects are investigated in detail in course of a follow-up observation of the primary matched object.

5.2 Halos versus peaks in noise-free κ maps

Let us first examine a probability that massive halos are identified as peaks in the noise-free κ maps. This ideal case can clarify the irreducible scatter in the relation between $\nu_{\rm lens}$ and $\nu_{\rm nfw}$, which

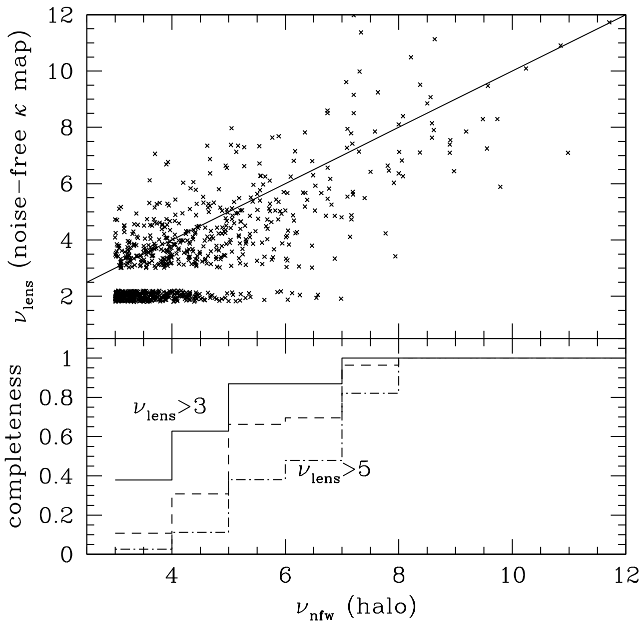

Figure 17. *Upper panel*: The correspondences between halos and peaks identified in the noise-free κ maps in $\nu_{\rm nfw}$-$\nu_{\rm lens}$ plane. The class-(i) and (ii) objects are shown (the class-(ii) objects are placed within a narrow track around $\nu_{\rm lens} \sim 2$, regardless of their true value). *Lower panel*: The histogram shows a fraction of halos that have the expected peak height in the range of $[\nu_{\rm nfw}, \nu_{\rm nfw}+1]$ indeed produces the lensing peaks above a given threshold ν_{th} in the κ map: $N(>\nu_{\rm lens}|\nu_{\rm nfw})/N(\nu_{\rm nfw})$. The sold, dashed and dot-dashed lines show the results for $\nu_{th} = 3$ 4 and 5, respectively. For example, the sold line shows that $\sim 60\%$ of all the halos with $\nu_{\rm nfw} = [4,5]$ are identified as peaks with $\nu_{\rm lens} > 3$ in the κ map.

Table 3. Summary of the completeness and efficiency. Here the fraction $f(i|j)$ is defined by $f(i|j) = N(i|j)/N(j)$.

Completeness	
noise-free	noisy
$f(\nu_{\rm lens} > 5\vert\nu_{\rm nfw} > 5) = 0.56$	$f(\nu_{\rm noisy} > 5\vert\nu_{\rm nfw} > 5) = 0.62$
$f(\nu_{\rm lens} > 4\vert\nu_{\rm nfw} > 5) = 0.77$	$f(\nu_{\rm noisy} > 4\vert\nu_{\rm nfw} > 5) = 0.81$
$f(\nu_{\rm lens} > 3\vert\nu_{\rm nfw} > 5) = 0.91$	$f(\nu_{\rm noisy} > 3\vert\nu_{\rm nfw} > 5) = 0.94$
$f(\nu_{\rm lens} > 4\vert\nu_{\rm nfw} > 4) = 0.54$	$f(\nu_{\rm noisy} > 4\vert\nu_{\rm nfw} > 4) = 0.63$
$f(\nu_{\rm lens} > 3\vert\nu_{\rm nfw} > 4) = 0.77$	$f(\nu_{\rm noisy} > 3\vert\nu_{\rm nfw} > 4) = 0.87$
Efficiency	
noise-free	noisy
$f(\nu_{\rm nfw} > 3\vert\nu_{\rm lens} > 3) = 0.73$	$f(\nu_{\rm nfw} > 3\vert\nu_{\rm noisy} > 3) = 0.28$
$f(\nu_{\rm nfw} > 3\vert\nu_{\rm lens} > 4) = 0.90$	$f(\nu_{\rm nfw} > 3\vert\nu_{\rm noisy} > 4) = 0.56$
$f(\nu_{\rm nfw} > 3\vert\nu_{\rm lens} > 5) = 0.95$	$f(\nu_{\rm nfw} > 3\vert\nu_{\rm noisy} > 5) = 0.83$

arises due to the simplified assumptions which we employ to compute $\nu_{\rm nfw}$ for a given halo (see §2).

Figure 17 shows the distribution of the class-(i) and (ii) halos in the $\nu_{\rm nfw}$-$\nu_{\rm lens}$ plane. Since the class-(ii) halos do not have a matched peak with height $\nu_{\rm lens} > 3$ in the κ map (although the halos have a high expected peak height of $\nu_{\rm nfw} > 3$), the halos are placed in a narrow locus around $\nu_{\rm lens} = 2$ for illustrative purpose. The distribution of the class-(i) halos shows a large scatter around the ideal relation $\nu_{\rm lens} = \nu_{\rm nfw}$ (shown by the solid line in the upper panel) over the range of ν we consider. It is worth noting that the distribution for a fixed $\nu_{\rm nfw}$ value is slightly biased toward lower $\nu_{\rm lens}$ values. We found that the mean and RMS of the difference, $\nu_{\rm lens} - \nu_{\rm nfw}$, are -0.24 and 1.2, respectively. Since no noise is added to the κ map in this case, the scatter and the bias are ascribed to the two effects; (1) the mass distribution within a halo is not spherical nor completely universal, causing deviations of the peak heights from the expected values computed from our simple model, and (2) a chance projection of structures along the same line-of-sight alters the lensing signal due to the halo. For the former, although we have so far used the mean relation for the halo concentration, given by eq. (2), it was shown in Jing (2000) that the halo concentrations among halos with a given mass obey the log-normal distribution with the variance $\sigma(\ln c_{\rm nfw}) = 0.2$ and the mean given by eq. (2). This roughly corresponds to a 20% RMS scatter in the $c_{\rm nfw}$ relation. Given the approximate relation $\kappa \propto c_{\rm nfw}^{1-1.5}$ for the peak height due to a massive halo (see §2), the RMS scatter in the $c_{\rm nfw}$ distribution translates into $20-30\%$ RMS scatters in the lensing signal $\nu_{\rm nfw}$ and therefore equivalently in the $\nu_{\rm lens}$-$\nu_{\rm nfw}$ relation. For example, for halos with $\nu_{\rm nfw} = 5$, the RMS of $\sigma_\nu \sim 1$ is caused. Second, the lensing projection due to physically unrelated structures along the same line-of-sight sight of a halo also contributes to the scatter in $\nu_{\rm lens}$. Following Hoekstra (2001), this scatter can be estimated from the cosmic weak lensing variance under the assumption that the halo and the large-scale structures are uncorrelated. For the Gaussian smoothing scale $\theta_G = 1'$, the amplitude of the (linear) convergence variance is $\sigma_\kappa(1') = 0.01$ for the ΛCDM model, corresponding to the RMS deviation of $\sigma_\nu = 0.5$ because of the noise $\sigma_{\rm noise}(1') = 0.02$ (see eq. (12)). Hence, these two effects can basically explain the amplitude of the scatter in the $\nu_{\rm lens}$-$\nu_{\rm nfw}$ relation in Figure 17.

We also argue that the systematic bias in the $\nu_{\rm lens} - \nu_{\rm nfw}$ relation could be explained by the following two effects. The first is the fact that more than half of the halos have $R < 1$ (§3.4, Figure 10). Since R positively correlates with $\nu_{\rm lens}/\nu_{\rm nfw}$ (see Figure C2 in Appendix C), it causes the bias. The second is the projection with a void region in the same line-of-sight which reduces the lensing signal (see Metzler et al. 2001; White et al. 2002; Padmanabhan et al 2003 for detailed study on the projection effect).

Let us turn to the class-(ii) halos in Figure 17. Among the 367 class-(ii) halos, there are 17 halos that are supposed to produce peaks with $\nu > 5$ in the κ maps if the halos have the NFW profile (i.e., $\nu_{\rm nfw} > 5$ for our notation). Why are these halos missing ? Figure 18 explains this in terms of deviation of the mass distribution within a halo from the spherically symmetric NFW profile. We again use the parameters Q and R to quantify the mass distribution within a halo (see equations (19) and (22), respectively): $Q/Q_{\rm NFW} < 1$ (> 1) characterizes a halo that has centrally more (or less) concentrated mass distribution than expected from the NFW profile, while $R > 1$ (< 1) describes that the mass distribution is elongated along (or perpendicular) to the line-of-sight ($R = 1$ for the spherical symmetric halo). Therefore, a halo with $Q/Q_{\rm NFW} > 1$ and/or $R < 1$ likely leads to a less lensing signal than expected from the NFW profile (see Appendix C for more detailed analysis of the relations between the halo shape and the amplitude of the lensing signal). The upper plane of Figure 18 shows the distribution of the class-(ii) halos in z–$Q/Q_{\rm NFW}$ plane, while the lower panel shows the distribution in z–R plane. For comparison, the figure also shows the distributions for the class-(i) halos with $5 < \nu_{\rm nfw} < 7.5$ by the cross symbols. From the lower panel, it is clear that the class-(ii) halos can be separated into two distinct subgroups; those which have $Q/Q_{\rm NFW} > 2$ (plotted by the filled triangles) or $Q/Q_{\rm NFW} < 2$ (plotted by the filled circles). We indeed find that halos with $Q/Q_{\rm NFW} > 2$ show clear signatures of

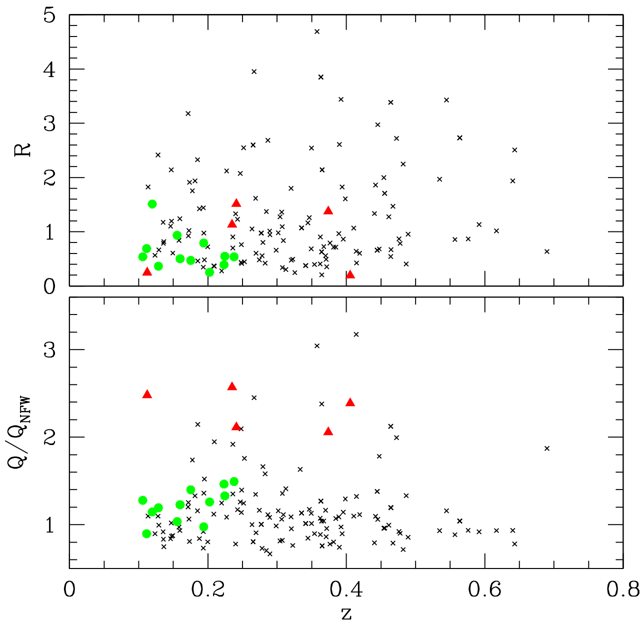

Figure 18. The scatter plot for the distribution of the halos in z–$Q/Q_{\rm NFW}$ plane (lower panel) and in z–R plane (upper panel). The filled circle and triangle symbols are for the class-(ii) halos with $\nu_{\rm nfw} > 5$. For comparison, the class-(i) halos with $5 < \nu_{\rm nfw} < 7.5$ are also plotted by the cross symbols. It is apparent from the lower panel that the class-(ii) halos can be separated into two subclasses: those which have $Q/Q_{\rm NFW} > 2$ are plotted by the filled triangles, while the rests are plotted by the filled circles.

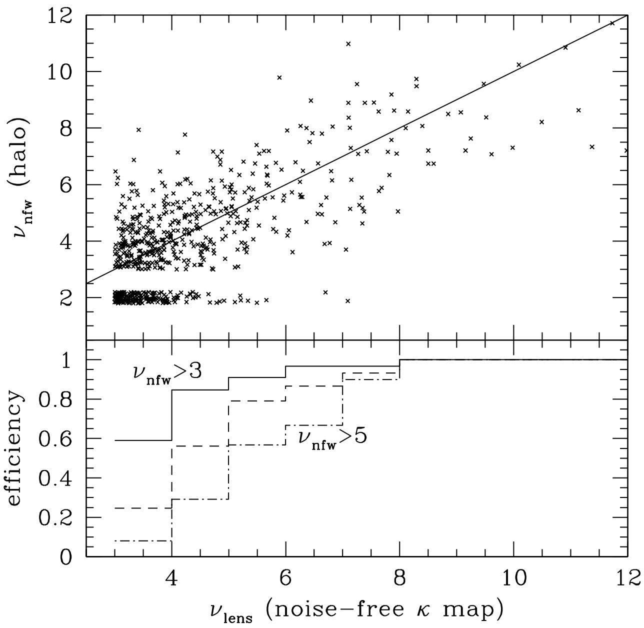

Figure 19. *Upper panel*: The correspondences between halos and peaks identified in the noise-free κ maps in $\nu_{\rm lens}$-$\nu_{\rm lens}$ plane, as in Figure 17. The class-(i) and (iii) objects are shown (the class-(iii) objects are placed within a narrow track around $\nu_{\rm nfw} \sim 2$, regardless of their true value). *Lower panel*: The fraction (representing the efficiency) of matched peaks with a corresponding $\nu_{\rm nfw}$ value larger than a certain threshold value, namely $N(>\nu_{\rm nfw}|\nu_{\rm lens})/N(\nu_{\rm lens})$ for three threshold values of $\nu_{\rm nfw} = 3$ (sold line), 4 (dashed line) and 5 (dot-dashed line).

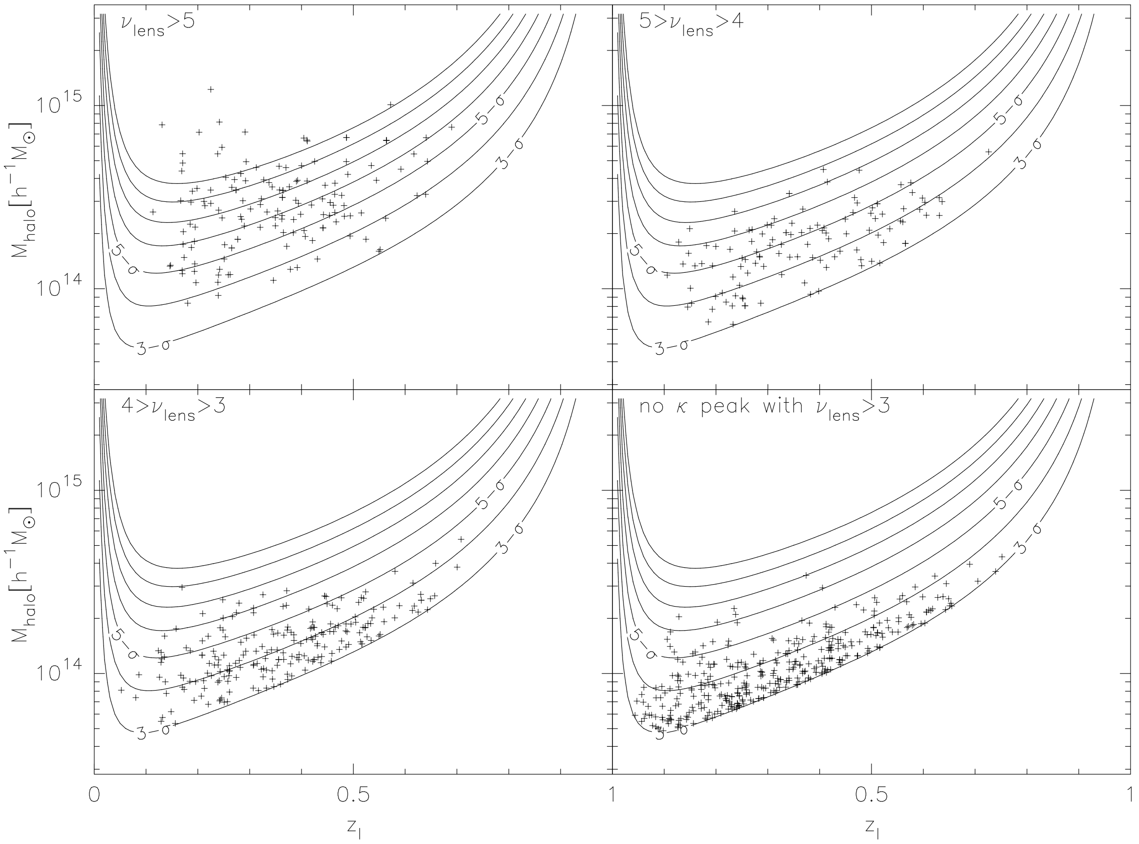

Figure 20. The scatter plot for the halos in the redshift-halo mass plane. The contours show the *expected* peak height $\nu_{\rm nfw}$ from 3 to 9 at interval of $\Delta\nu_{\rm nfw} = 1$. The class-(i) halos matched with peaks identified in *noise-free* κ maps are plotted in the upper-left ($\nu_{\rm lens} > 5$), upper-right ($5 > \nu_{\rm lens} > 4$) and lower-left panels ($4 > \nu_{\rm lens} > 3$). The lower-right panel shows the scatter plot for the class-(ii) "*missing halos*".

substructures or on-going merging, resulting in the extended mass distribution (see Figure A1 for the example in the κ map). The remaining objects with $Q/Q_{\rm NFW} < 2$ tend to be located at a low redshift ($z < 0.25$), where the lensing efficiency is relatively small for the source redshift $z_s = 1$ we consider, and have a small R, mostly $R < 1$. The examples are shown in Figures A2 and A3. These halos typically have prominent substructures and the whole mass distribution within the halo is indeed elongated along the perpendicular direction to the line-of-sight. Except for such irregular systems, almost all massive halos with $\nu_{\rm nfw} > 5$ generate a high peak with $\nu_{\rm lens} > 3$. It is important to note that the distribution of the class-(ii) halos is not clearly separated from that of the class-(i) halos in Figure 18, reflecting the fact that the lensing signal is also affected by the projection effect.

In the lower panel of Figure 17, the histogram shows the fraction of halos, which cause lensing peaks above a given threshold ν_{th} in the κ map, among all the halos in a given range of $[\nu_{\rm nfw}, \nu_{\rm nfw} + 1]$: $N(> \nu_{\rm lens}|\nu_{\rm nfw})/N(\nu_{\rm nfw})$. This represents the *completeness* of the weak lensing halo search. For example, only $\sim$ 60% of all the halos in $\nu_{\rm nfw} = [4, 5]$ generate peaks with $\nu_{\rm lens} > 3$ in the κ map. To increase the completeness requires lowering the threshold ν_{th}. It is also useful to show the integrated fraction over the expected peak height $\nu_{\rm nfw}$: $f(\nu_{\rm lens} > \nu_{th}|\nu_{\rm nfw} > j) = N(\nu_{\rm lens} > \nu_{th}|\nu_{\rm nfw} > j)/N(\nu_{\rm nfw} > j)$. The results are summarized in Table 3. It is clear that only about half of halos with $\nu_{\rm nfw} > 5$ produces peaks with $\nu_{\rm lens} > 5$ in the κ maps, and that 77 percent have $\nu_{\rm lens} > 4$. The completeness becomes worse for halos with lower $\nu_{\rm nfw}$ values, as expected. Note that some of the halos with $\nu_{\rm lens}$ much smaller than $\nu_{\rm nfw}$ are irregular systems or un-relaxed systems, and therefore the completeness is likely to be improved for samples of regular, well relaxed halos. It should be noted that the noise increases the completeness (see §5.4), and therefore the results in Figure 17 and Table 3 can be regarded as a conservative estimate.

Figure 19 shows the results for the class-(i) and (iii) objects in $\nu_{\rm lens}$-$\nu_{\rm nfw}$ plane, similarly as in Figure 17. Class (iii) objects are the peaks with $\nu_{\rm lens} \geqslant 3$ in the lensing map, but do not have the corresponding halos in the halo catalog (contains only halos with $\nu_{\rm nfw} > 3$), which are placed around $\nu_{\rm nfw} \sim 2$ for illustrative purpose. Among the class-(iii) objects there are 8 events with $\nu_{\rm lens} > 5$ and we call these "false peaks". We carefully looked into each case in the κ map and searched for a possible related halo in the halo catalog. We found that the 5 events are associated with substructure of massive halos or the secondary local peaks of merger systems (note that the peaks are separated from the primary peak of the halo center by more than 12 pixels). Figure A4 shows an example in the κ map. The remaining 3 peaks are due to a chance projection of two moderately massive halos at different redshifts (Figure A5 shows the one example). Therefore, except for the three chance projection systems, the *false peaks* are associated with a real massive halo.

The lower panel of Figure 19 shows what percentage of the peaks in a given range of $[\nu_{\rm lens}, \nu_{\rm lens} + 1]$ is associated with halos whose $\nu_{\rm nfw}$ is larger than a certain threshold value: $N(> \nu_{\rm nfw}|\nu_{\rm lens})/N(\nu_{\rm lens})$. This represents the *efficiency* of the weak

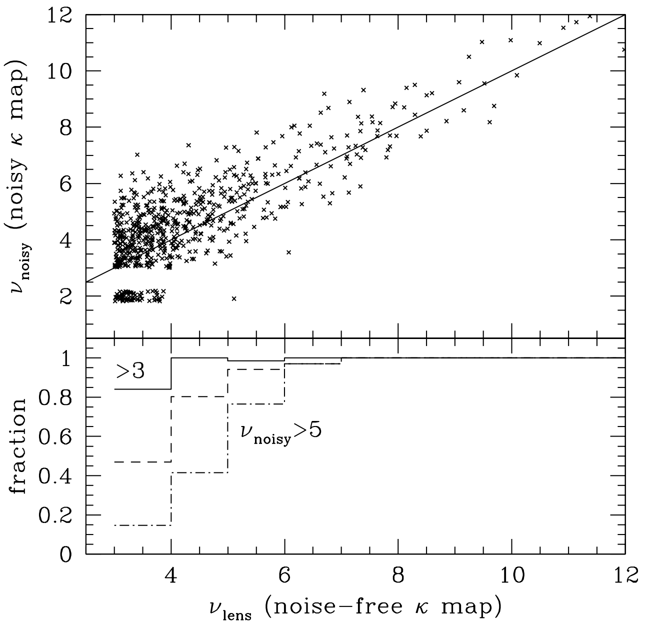

Figure 21. *Upper panel*: The correspondences of peak heights between identified in the noise-free and noisy κ maps. The peaks, which have $\nu_{\rm lens} > 3$ but are missed in the noisy κ map or have $\nu_{\rm noisy} < 3$, are placed within a narrow locus at $\nu_{\rm noisy} \sim 2$, regardless of their true $\nu_{\rm noisy}$ value. *Lower panel*: The fraction of matched peaks, $N(>\nu_{\rm noisy}|\nu_{\rm lens})/N(\nu_{\rm lens})$ for three threshold values of $\nu_{\rm noisy} = 3$ (sold line), 4 (dashed line) and 5 (dot-dashed line).

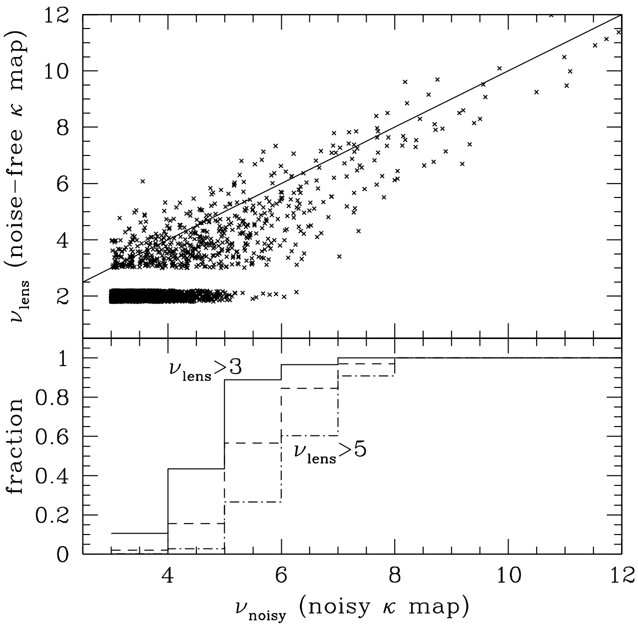

Figure 22. *Upper panel*: The same plot as in Figure 21, but the x- and y-axises are exchanged to highlight the contamination by false peaks. The peaks, which have $\nu_{\rm noisy} > 3$ but no paired peak with $\nu_{\rm lens} > 3$, are placed within the locus at $\nu_{\rm lens} \sim 2$, regardless of their true $\nu_{\rm lens}$ value. *Lower panel*: The fraction of matched peaks, $N(>\nu_{\rm lens}|\nu_{\rm noisy})/N(\nu_{\rm noisy})$ for three threshold values of $\nu_{\rm lens} = 3$ (sold line), 4 (dashed line) and 5 (dot-dashed line).

lensing halo search. Since no noise is added to the κ maps, the efficiency given here should be regarded as an optimistic estimate. Table 3 shows the integrate fraction over the peak height: $f(>\nu_{\rm nfw}|\nu_{\rm lens} > \nu_{th}) = N(>\nu_{\rm nfw}|\nu_{\rm lens} > \nu_{th})/N(\nu_{\rm lens} > \nu_{th})$. Clearly the efficiency is very high. If one sets the detection threshold by $\nu_{\rm lens} > 5$, 95% of all the peaks correspond to real halos with $\nu_{\rm nfw} > 3$, and among the rest 8 peaks, 5 peaks are secondary peaks associated with a massive halo and 3 peaks are due to chance projections as discussed in above. Therefore, in the absence of the noise, contamination (a fraction of false peaks) is negligibly small for detection threshold $\nu_{\rm lens} > 5$.

Figure 20 shows the scatter plot of the class-(i) and class-(ii) halos in the redshift–halo mass plane. The contours show tracks of the expected peak height $\nu_{\rm nfw}$ from 3 to 9 with an interval of $\Delta\nu_{\rm nfw} = 1$. The class-(i) halos matched with peaks identified in *noise-free* κ maps are plotted in the upper-left ($\nu_{\rm lens} > 5$), upper-right ($5 > \nu_{\rm lens} > 4$) and lower-left panels ($4 > \nu_{\rm lens} > 3$), respectively. The lower-right panel shows the scatter plot for the class-(ii) halos, namely "*missing halos*". Importantly, the peaks correspond to halos over a wide range of masses due to the projection effect and the individuality of the halo mass distribution. We also note that in the distribution of the *missing halos* (lower-right panel) no strong tendency with redshift is observed, and thus the completeness would not significantly vary with redshift.

5.3 Effects of the noise on the lensing peaks

Before examining correspondences between peaks identified in the noisy κ maps and halos in the halo catalog, we qualitatively examine how the noise alters the height of peaks due to halos and generates false peaks in the lensing map.

Matching between the noise-free peaks and the noisy peaks was done in the same manner described in §5.1. In what follows, the peaks classified in the class-(i-iii) (its analogy to $\nu_{\rm lens}$-$\nu_{\rm noisy}$ correspondence) are considered. Again, we only deal with peaks with $\nu > 3$.

Figures 21 and 22 show the relations between $\nu_{\rm lens}$ and $\nu_{\rm noisy}$, similarly as in Figures 17 and 19. We emphasize that the statistical properties of the $\nu_{\rm lens}$-$\nu_{\rm noisy}$ relation do not follow the Gaussian distribution, even though the Gaussian noise is added. The reason is as follows. The noise not only alters the height of peaks from massive halos but also shift the peak position. For example, if a large positive noise is accidentally added on a neighboring pixel around the original peak position, the pixel could be identified as a peak that is even higher than the original peak. Therefore, the distribution of $\nu_{\rm noisy}$'s is not simply expressed as the convolution of that of $\nu_{\rm lens}$'s with the Gaussian noise. The $\nu_{\rm lens}$-$\nu_{\rm noisy}$ relation becomes asymmetric and is biased toward large $\nu_{\rm noisy}$ values. This explains the asymmetric $\nu_{\rm lens}$-$\nu_{\rm noisy}$ relation clearly shown in Figures 21 and 22. The mean and RMS of the difference, $\nu_{\rm noisy} - \nu_{\rm lens}$, among the class-(i) objects with $\nu_{\rm lens} > 4$ (this restriction is imposed in order to avoid an incomplete sampling of low $\nu_{\rm noisy}$ pairs) are 0.31 and 0.90, respectively. Therefore the peak heights of massive halos identified in a noisy κ map are, on average, boosted by the noise. This bias partly accounts for the excess in the peak number counts over the simple theoretical prediction, eq. (16), as shown in §4.2.

The class-(ii) objects here correspond to the *missing peaks*, the peaks that have $\nu_{\rm lens} > 3$ but are absent in the corresponding noisy κ map or have $\nu_{\rm noisy} < 3$. Except for one peak with $\nu_{\rm lens} = 5.1$, the missing peaks sit in the range of $\nu_{\rm lens} \geqslant 4$. These peaks are likely to be erased or their heights are decreased by the addition of the negative noise. The one exception (the peak with $\nu_{\rm lens} = 5.1$ at the missing peak locus) is a local peak associated with a

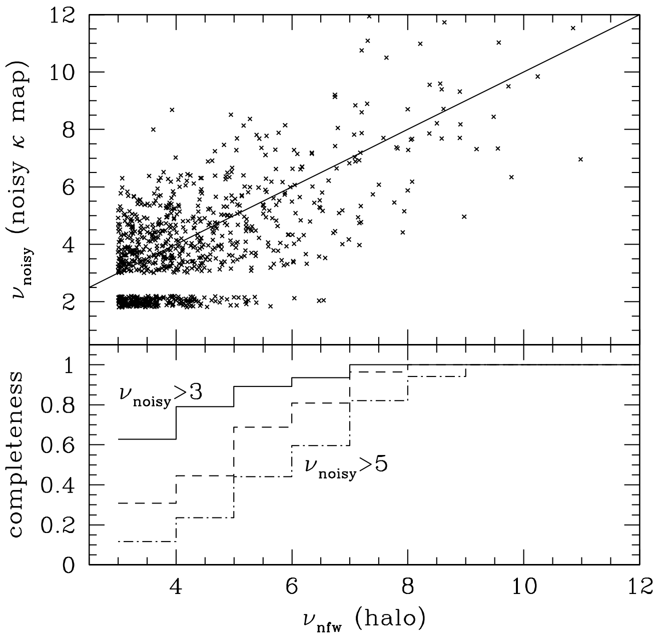

Figure 23. Same as Figure 17 but for the correspondence between halos and peaks identified in the noisy κ maps.

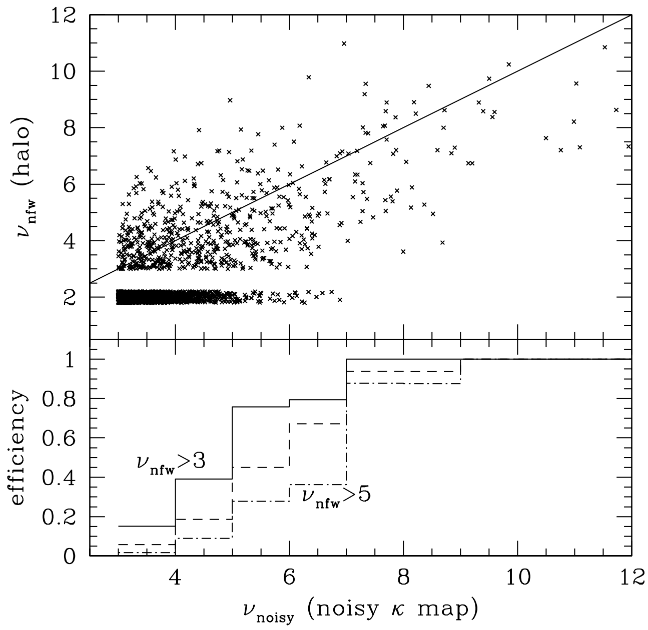

Figure 24. Same as Figure 19 but for the correspondence between halos and peaks identified in the noisy κ maps.

substructure of a massive halo which disappears in the noisy κ map. We may, therefore, safely conclude that more than 80% of the peaks with $\nu_{\rm lens} \geqslant 3$ in the noise-free map remain in the noisy κ map.

Next, we consider the *false peaks*, the peaks that are identified in the noisy κ map with $\nu_{\rm noisy} > 3$ but does not correspond to peaks in the noise-free κ map, which are placed around $\nu_{\rm lens} \sim 2$ in the upper panel of Figure 22. A large fraction of the false peaks, especially for $\nu_{\rm noisy} < 4$, are the false peaks generated by the noise (see §4 for details), and a small fraction (especially those with relatively high $\nu_{\rm noisy}$) is associated with real peaks on which a large noise is accidentally added. Actually, there are 14 objects with $\nu_{\rm noisy} > 5$ in the *false peaks* locus. All of those have a corresponding peak in the noise-free κ map with low peak height $1.5 < \nu_{\rm lens} < 2.9$ and a relatively large noise of $2 \sim 3.5\sigma$ is accidentally added on those peaks. Therefore, all peaks with $\nu_{\rm noisy} > 5$ identified in the noisy κ map are associated with real peaks in the noise-free κ map. The lower panel of Figure 22 shows the fraction of the matched peaks. As this clearly indicates, the fraction of the false peaks rapidly increases with decreasing $\nu_{\rm noisy}$. It immediately follows from this that in order to reduce the fraction of the contamination, a high threshold value, $\nu_{\rm noisy} > 4$ at least, is required.

5.4 Halos versus peaks in noisy κ maps

In this subsection, we examine correspondences between halos in the halo catalog and peaks in the κ map including the noise due to the intrinsic ellipticities. Figure 23 shows the distribution of the class-(i) and (ii) halos in $\nu_{\rm nfw}$-$\nu_{\rm noisy}$ plane, similarly as in Figure 17. The comparison with Figure 17 reveals that the noise increases the scatter in the $\nu_{\rm noisy}$-$\nu_{\rm nfw}$ relation. This effect is in a biased way: the number of halos with $\nu_{\rm noisy} > \nu_{\rm nfw}$ is enhanced relative to that of halos with $\nu_{\rm lens} > \nu_{\rm nfw}$. Interestingly, the bias leads the *completeness* for the weak lensing halo search to be improved by the noise, as summarized in Table 3. About 81 (63) percent of massive halos with $\nu_{\rm nfw} > 5$ (> 4) are identified as peaks with $\nu_{\rm noisy} > 4$ in the noisy maps. This is one of the most important results of this paper, indicating that a high completeness of the weak lensing halo search could be attained in a realistic data.

There are 13 *missing* halos that have $\nu_{\rm nfw} > 5$ but $\nu_{\rm noisy} < 3$. We look into each case in κ map and find that 11 halos out of 13 are irregular systems such as un-relaxed systems having substructures or on-going merger. Therefore, the *completeness* of the weak lensing halo search for regular, well relaxed systems would be higher than the estimate summarized in Table 3. The remaining two *missing* halos, which have $\nu_{\rm nfw} = 5.3$ and 5.4, are those which accidentally meet a large negative noise and their κ values are reduced to be below $\nu_{\rm noisy} = 3$. The fraction of such halos over all halos with $\nu_{\rm nfw} > 5$ is 0.8% (2 out of 250 halos), which is indeed very small. Therefore, we can safely conclude that almost all halos with $\nu_{\rm nfw} > 5$ generate peaks with $\nu_{\rm noisy} > 3$ in the presence of the noise.

Figure 24 shows the distribution of the class-(i) and (iii) objects in $\nu_{\rm noisy}$-$\nu_{\rm nfw}$ plane, similarly as in Figure 19. Since the noise generates false peaks in the κ map, the *efficiency* becomes worse than the noise-free case (see Table 3). The fraction of contamination by the false peaks is larger for a lower peak height because the noise generates relatively lower peaks, mostly $\nu_{\rm noisy} < 4$. Therefore, if $\nu_{\rm noisy} = 3$ is employed as the detection threshold, the efficiency becomes only 23%. Note that since we only consider halos with $\nu_{\rm nfw} > 3$, some fraction of *missing peaks* could be associated with halos with $\nu_{\rm nfw} < 3$. On the other hand, the efficiencies for higher detection thresholds of $\nu_{\rm noisy} = 4$ and 5 are reasonably high, 56% and 83%, respectively.

From Table 3, it is clear that a better *efficiency* achieved by setting a higher detection threshold is a "trade-off" for a worse *completeness*. We also note that the peak counts vary rapidly with increasing the threshold. For example, the counts $N(\nu > 4)$ are twice as large as $N(\nu > 5)$ (see §4). Therefore, the detection threshold should be determined such that the *efficiency* and *completeness* are optimized for specific survey strategies. The results we have so far shown indicate that $\nu_{\rm noisy} = 4 \sim 5$ is reasonably optimal for currently typical weak-lensing surveys. To be more specific, the results

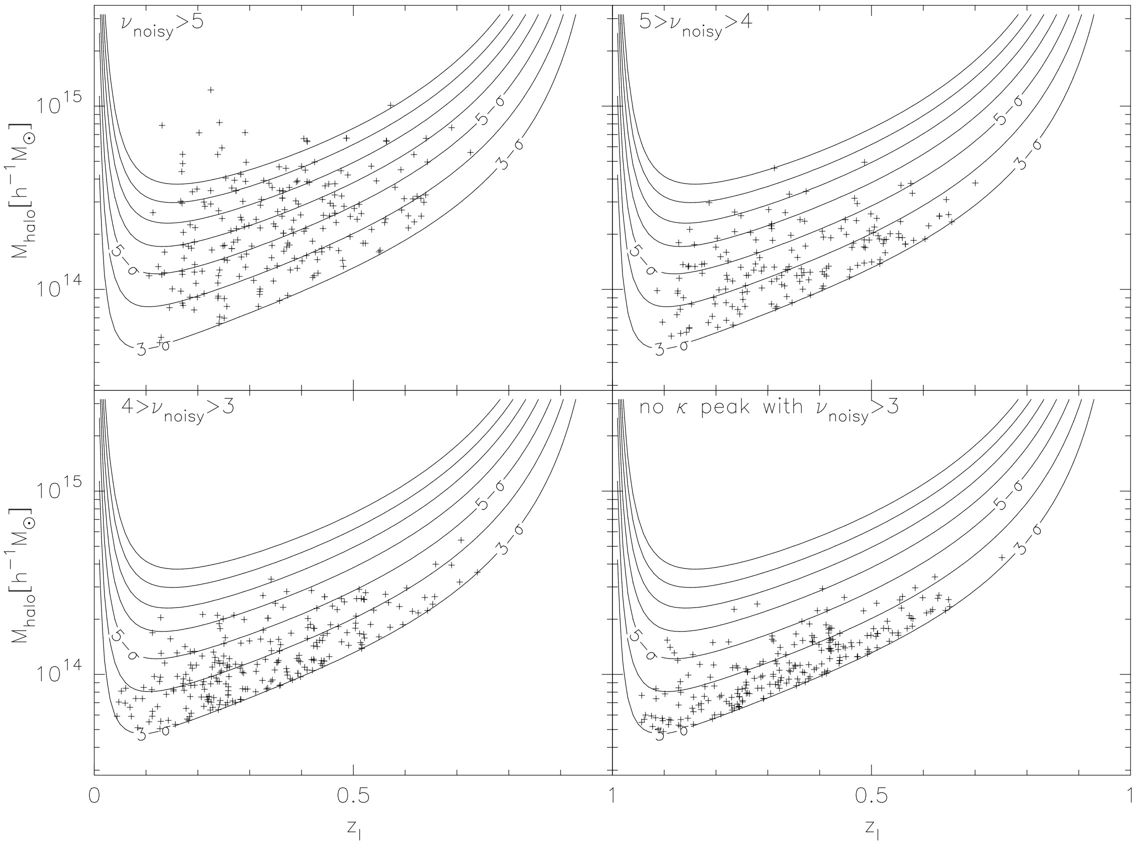

Figure 25. Same as Figure 20 but for halos matched (do not matched, for lower-right panel) with peaks identified in *noisy* κ maps.

from the simulated κ maps for the ΛCDM model indicate that, if one sets the detection threshold to $\nu_{\rm noisy} = 4$, the mean number of peaks is $N_{\rm peak}(\nu_{\rm noisy} > 4) = 65$ per 10 deg^2. The 36 peaks out of 65 are due to real halos with $\nu_{\rm nfw} > 3$ and the remaining 29 peaks are likely to be false peaks due to the noise (some fraction of the false peaks might be signals from halos with $\nu_{\rm nfw} < 3$). On the other hand, if one uses a higher detection threshold $\nu_{\rm noisy} = 5$, the mean number of peaks is $N_{\rm peak}(\nu_{\rm noisy} > 5) = 25$ per 10 deg^2, and the contamination rate is reduced down to only 17%. Thus, 21 peaks out of 25 are signals from real halos with $\nu_{\rm nfw} > 3$. Concerning the completeness, the mean number of halos with $\nu_{\rm nfw} > 4$ is $N_{\rm halo}(\nu_{\rm nfw} > 4) = 37$ per 10 deg^2, and the 63% of halos (23 halos out of 37) are detected with $\nu_{\rm noisy} > 4$ on average. The completeness is better for higher $\nu_{\rm nfw}$ halos: for halos with $\nu_{\rm nfw} > 5$, the mean number is $N_{\rm halo}(\nu_{\rm nfw} > 5) = 19$ per 10 deg^2, where 81% of the halos (15 halos out of 19) are detected with $\nu_{\rm noisy} > 4$, and 12 halos have even high lensing signal of $\nu_{\rm noisy} > 5$.

Figure 25 shows the scatter plot for the class-(i) and class-(ii) halos in the redshift–halo mass plane. The class-(i) halos matched with peaks identified in noisy κ maps are plotted in the upper-left ($\nu_{\rm lens} > 5$), upper-right ($5 > \nu_{\rm lens} > 4$) and lower-left ($4 > \nu_{\rm lens} > 3$) panels. The lower-right panel shows the scatter plot for the class-(iii) "missing halos". From comparison of this figure with Figure 20, one may find that more halos pass a certain detection threshold than in the noise-free map, because of the systematic bias due to the noise. Another important point is that the peak height in the noisy κ map is a poor estimator of the halo mass. For example, masses of the halos detected with $4 < \nu_{\rm noisy} < 5$ span over an order of magnitude. Even in a narrow redshift range such as $0.3 < z < 0.4$, there still exits a significant scatter in the halo mass. Note that we do not plot halos with $\nu_{\rm nfw} < 3$, which may cause a larger scatter toward small mass ranges. It should be also noted that in the distribution of the missing halos (lower-right panel) no strong tendency with redshift is seen, indicating that the completeness would not vary significantly with redshift.

So far we have examined the relation between halos and peaks in a κ map in terms of the peak height instead of the halo mass because the lensing observable is determined by combination of the halo mass, the redshift and the noise level, rather than by the halo mass alone. Nevertheless, it is interesting to see what mass range of halos produces the peaks in the noisy κ maps, which is shown in Figure 26 similarly as in Figure 23. Again only halos with $\nu_{\rm nfw} > 3$ are considered. As seen in the upper panel, the peaks with a given height are caused by halos with a wide range of the masses. The lower panel shows the completeness as a function of the halo mass. The completeness declines toward lower mass and toward higher detection threshold. Table 4 gives a summary of the completeness. For a detection threshold $\nu_{\rm noisy} = 4$, about a half of halos with $M_{\rm halo} > 1 \times 10^{14} h^{-1} M_\odot$ is detected, and 70 percent of halos with $M_{\rm halo} > 2 \times 10^{14} h^{-1} M_\odot$ are detected. These results are consistent with Figure 6 in White et al. (2002)[3].

[3] Note that their definition of the smoothing scale is different from ours; the full width half of maximum σ is employed in White et al. (2002), which roughly relates to our smoothing scale θ_G as $\sigma \simeq 1.66\theta_G$

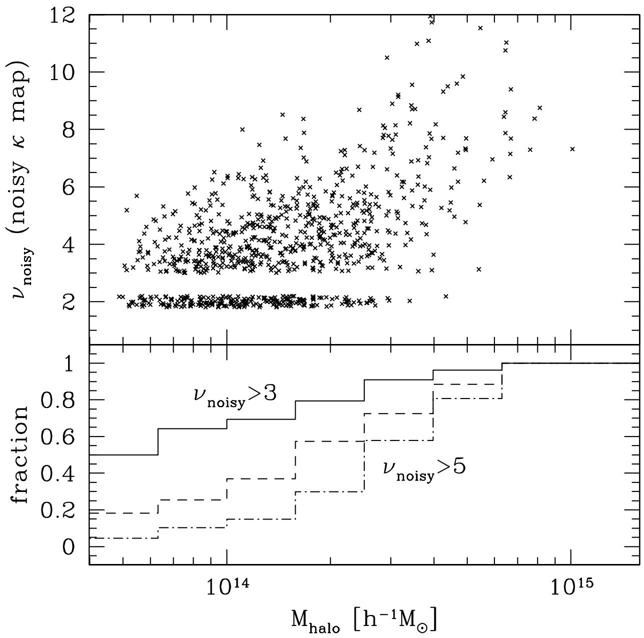

Figure 26. Same as Figure 23 but the halo mass is used instead of the *expected* peak height of $\nu_{\rm nfw}$. Note that only halos with $\nu_{\rm nfw} > 3$ are considered.

Table 4. Completeness of the weak lensing dark matter halo search. Here the fraction $f(i|j)$ is defined by $f(i|j) = N(i|j)/N(j)$. Only halos with $\nu_{\rm nfw} > 3$ are considered.

Completeness
$f(\nu_{\rm noisy} > 5 \vert M_{\rm halo} > 2 \times 10^{14}) = 0.53$
$f(\nu_{\rm noisy} > 4 \vert M_{\rm halo} > 2 \times 10^{14}) = 0.70$
$f(\nu_{\rm noisy} > 3 \vert M_{\rm halo} > 2 \times 10^{14}) = 0.89$
$f(\nu_{\rm noisy} > 5 \vert M_{\rm halo} > 1 \times 10^{14}) = 0.31$
$f(\nu_{\rm noisy} > 4 \vert M_{\rm halo} > 1 \times 10^{14}) = 0.52$
$f(\nu_{\rm noisy} > 3 \vert M_{\rm halo} > 1 \times 10^{14}) = 0.77$

6 SUMMARY AND DISCUSSION

We have investigated various aspects of the weak lensing cluster survey employing both analytic descriptions of the dark matter halos and the mock data of weak lensing surveys generated from numerical experiments which combines the weak lensing ray-tracing with the dark matter halo catalog. Our major findings are summarized as follows;

(1) In §2, we examined the expected properties of weak lensing halos using analytical descriptions of the dark matter halos, including the universal profile (Navarro et al. 1996; 1997) and the Press-Schechter halo mass function (Press & Schechter 1974: Sheth & Tormen 1999). We find that the Gaussian smoothing scale of $\theta_G \simeq 1$ arcmin gives the largest expected weak lensing halo counts (which may however depend on the source redshift and noise properties). We compute the selection function of the weak lensing cluster survey and examine, in detail, the mass and redshift distribution of the weak lensing halos. We find the detectability of halos depends not only on the mass but also strongly on the redshift.

(2) In §3.4, we test the model prediction of the weak lensing halo counts developed by Kruse & Schneider (2000) and Bartelmann et al. (2001) against the mock halo catalog, and find a good agreement. We also find a large scatter in the numbers of weak lensing halos within 4 square degrees field, which is larger than the Poisson fluctuation. This may be explained by the strong clustering of the massive halos.

(3) In §4, we test the model prediction of the peak counts against the mock weak lensing data. It is found that a systematic bias is induced by the noise due to intrinsic galaxy ellipticities. This bias increases the peak counts, and hence the model prediction ought to underestimate the counts. We develop the correction scheme in an empirical manner in Appendix B. The corrected theoretical model counts agree well with the results of the mock catalogs.

(4) In §5.2, using the mock weak lensing data combined with the halo catalog, we examine the correspondence between halos and peaks identified in the noise-free κ map. The aim of this subsection was to examine the effects of the individuality of halos and the projection effects. We find that these effects produce not only a large scatter in the $\nu_{\rm lens}$-$\nu_{\rm nfw}$ relation but also bias. The mean and RMS of the difference $\nu_{\rm nfw} - \nu_{\rm lens}$ are -0.24 and 1.2, respectively. The scatter caused by these effects is comparable to that due to the noise. We argue that possible reasons for the negative mean value are the fact that the more than half of all halos are elongated to the direction perpendicular to the line-of-sight and a population of unrelaxed, less centrally concentrated halos. The latter is likely due to structure formation activities such like on-going mergers. Also the projection of large under-dense regions may partially account for the trend. It is also found that the chance projection of massive halos in the same line-of-sight is very rare, and does not cause many false high lensing signals.

(5) In §5.3, we examine the correspondence between noise-free peaks and noisy peaks. The aim of the sub-section was to look into how the noise affects the height of the peaks and how many false peaks with a high peak height are generated. We find that the $\nu_{\rm lens} - \nu_{\rm noisy}$ distribution is biased toward large $\nu_{\rm noisy}$ values. The mean and RMS of the differences, $\nu_{\rm noisy} - \nu_{\rm lens}$, among the matched peaks with $\nu_{\rm lens} > 4$ and $\nu_{\rm noisy} > 4$ are 0.31 and 0.90, respectively. Thus the noise not only generates the scatter but also systematically 'boosts' the peak heights. We find that almost all the peaks identified in the noise-free κ map with $\nu_{\rm lens} > 4$ are identified in the noisy κ map, thus the noise rarely erases the high peaks. All the peaks with $\nu_{\rm noisy} > 5$ identified in the noisy κ map are associated with real peaks in the noise-free κ map, whereas most of the false peaks (due to the noise) have a relatively lower peak height $\nu_{\rm noisy} < 4$.

(6) In §5.4, we examine the correspondence between the halos and peaks identified in the noisy κ map, paying a special attention to the *efficiency* and *completeness* of the weak lensing halo survey. We found that the detection threshold of $\nu_{th} = 4 \sim 5$ gives an optimal balance between the efficiency and completeness. We find that about 81 (63) percent of massive halos with $\nu_{\rm nfw} > 5$ (> 4) are identified with a high peak height of $\nu_{\rm noisy} > 4$. This indicates that the completeness of the weak lensing cluster survey is reasonably high. We find that the efficiencies for $\nu_{\rm noisy} = 4$ and 5 are 56% and 83%, respectively. Therefore, by selecting a moderately high detection threshold, a relatively high efficiency is attainable.

(7) In §5.4, it is also found that for a detection threshold of $\nu_{\rm noisy} = 4$ about a half of $\nu_{\rm nfw} > 3$ halos with $M_{\rm halo} > 1 \times 10^{14} h^{-1} M_\odot$ and 70 percent of those with $M_{\rm halo} > 2 \times 10^{14} h^{-1} M_\odot$ are above the threshold.

Weak lensing cluster search technique explored in this paper can be directly applied to data obtained by on-going/future wide field surveys as demonstrated by Miyazaki et al. (2002). Expanding the pilot 2.1 square degree survey (Miyazaki et al. 2002), a wide field weak lensing survey (Suprime33, PI: S. Miyazaki) is being carried out with the wide field prime focus camera of Subaru telescope (Miyazaki et al. in preparation). The Suprime33 will observe a 33 square degrees area in total with the limiting magnitude $R = 25.5$ (which provides $n_g \gtrsim 30$ and $\langle z_s \rangle \simeq 1$). The expected number of clusters, which the Suprime33 will locate, is 70 (120) for the threshold $\nu > 5$ ($\nu > 4$). The CFHT Legacy Survey[4] will significantly enlarge the survey area. Its "wide" survey will observe a 170 square degrees area in total with the limiting magnitude $i' = 25.5$ (which also provides $n_g \gtrsim 30$ and $\langle z_s \rangle \simeq 1$). The expected number of clusters is 360 (600) for $\nu > 5$ ($\nu > 4$), and thus it will be an invaluable data for studies in astronomy and cosmology. Although in this paper, we have primarily considered weak lensing surveys that current ground-based telescopes are aimed at, future wide field surveys exploiting a space telescope will enable to accurately measure the shape of distant very small galaxy images, which significantly improves the ability of weak lensing cluster surveys and allows to detect lower mass and/or higher redshift clusters.

Although in this paper we have considered only the Gaussian smoothing, it is, in principle, possible to enhance the S/N of the detection by a suitable choice of the smoothing function (White et al. 2002; Padmanabhan et al. 2003). Padmanabhan et al. (2003) proposed the function of $W(\theta) = (1 + \theta/\theta_c)^{-2}$ with $\theta_c \sim 1$ arcmin, which is motivated by the asymptotic behavior of the outer part of the projected NFW profile. Such matched filters may improve the S/N if the dark matter distribution of cluster is well close to the NFW profile. However, it is not clear how well it works for halos whose mass distribution deviates from the NFW profile, and thus it is not clear how much the efficiency and completeness are improved. This issue will be studied in a future work.

ACKNOWLEDGMENTS

We are grateful to Bhuvnesh Jain for many valuable discussions. We would like to thank Satoshi Miyazaki for useful discussions. T.H. and N.Y. thank University of Pennsylvania for the warm hospitality during their visit where this work was initiated. T.H. and N.Y. acknowledge supports from Japan Society for Promotion of Science (JSPS) Research Fellowships. The N-body simulations used in this work were carried out by the Virgo Consortium at the computer center at Max-Planck-Institut, Garching (http://www.mpa-garching.mpg.de/NumCos). Numerical computations presented in this paper were partly carried out at ADAC (the Astronomical Data Analysis Center) of the National Astronomical Observatory, Japan.

REFERENCES

Bardeen J. M., Bond J. R., Kaiser N., Szalay A. S. 1986, ApJ, 304, 15
Bartelmann M., 1996, A&A, 313, 443
Bartelmann M., King, L. J., Schneider P., 2001, A&A, 378, 361
Bartelmann M., Schneider P., 1992, A&A, 259, 413
Bartelmann M., Schneider P., 2001, Phys. Rep., 340, 291
Bond, J. R., Efstathiou, G., 1987, MNRAS, 226, 655
Bullock J. S., Kolatt T. S., Sigad Y., Somerville R. S., Kravtsov A. V., Klypin A. A., Primack J. R., Dekel A. 2001, MNRAS, 321, 559
Hamana, T., Mellier, Y. 2001, MNRAS, 169, 176
Hamana T., Yoshida N., Suto Y., 2002, ApJ, 568, 455
Henry, J. P. 2000, ApJ, 534, 565
Hockney, R. W., Eastwood, J. W., 1988, Computer Simulation Using Particles (Adam Hilger, Bristol)
Hoekstra H., 2001, A&A, 370, 743
Jain, B., Seljak, U., White, S. D. M., 2000, ApJ, 530, 547
Jain, B., Van Waerbeke, L., 2000, ApJ, 530, L1
Jenkins A., Frenk C. S., White S. D. M., Colberg J. M., Cole S., Evrard A. E., Couchman H. M. P., Yoshida N., 2001, MNRAS, 321, 372
Jing, Y. P., 2000, ApJ, 535, 30
Kaiser, N., Squires, G., 1993, ApJ, 404, 441
Kruse, G., Schneider, P., 2000, MNRAS, 318, 321
Macfarland, T., Couchman, H. M. P., Pearce, F. R., Pichlmeier, J., 1998, New Astronomy, 3, 687
Mellier Y., 1999, ARA&A, 37, 127
Metzler C. A., White M., Loken C., 2001, ApJ, 547, 560
Miyazaki, S., et al., 2002, ApJ, 580, L97
Nakamura, T. T., & Suto, Y. 1997, Prog. Theor. Phys., 97, 49
Navarro J., Frenk C., White S. D. M. 1996, ApJ, 462, 563
Navarro J., Frenk C., White S. D. M. 1997, ApJ, 490, 493
Padmanabhan N., Seljak U., Pen, U. L., 2003, New Astronomy, 8, 581
Press W. H., Schechter P., 1974, ApJ, 187, 425
Schneider, P., Ehlers, J., Falco, E. E., 1992, *Gravitational Lenses*, (Heidelberg: Springer Verlag)
Seljak, U., Zaldarriaga, M. 1996, ApJ, 469, 437
Sheth R. K., Tormen G., 1999, MNRAS, 308, 119
Takada M., Jain B., 2003, MNRAS, 340, 580
Reblinsky K., Bartelmann M., 1999, A&A, 345, 1
Van Waerbeke, L., 2000, MNRAS, 313, 524
Vale, C., White, M., 2003, ApJ, 592, 699
White, M., Van Waerbeke, L., Mackey, J., 2002, ApJ, 575, 640
Wittman, D., Tyson, J. A., Margoniner, V. E., Cohen, J. G., Dell'Antonio, I. P., 2001, ApJ, 557, L89
Wright, C. O., Brainerd, T. G., 2000, ApJ, 534, 34
Yoshida, N., Sheth, R., Diaferio, A., 2001, MNRAS, 328, 669

APPENDIX A: VISUAL APPEARANCES OF SYSTEMS WITH IRREGULAR SIGNALS

Here we present some κ maps, in which *missing halos* (the class-(ii)) or *doubtful peaks* (the class-(iii)) with high signals ($\nu > 5$) exists, for examples of irregular systems. Figures A1-A5 show the (noise-free) convergence maps smoothed with Gaussian window function with $\theta_G = 1$ arcmin. Pluses denote the center-of-mass position of halos concerned and the circles show their virial radius. Crosses denote the position of peaks.

Figures A1-A3 show three examples of *missing halos* with the expected peak value $\nu_{\rm nfw} > 5$. Such high $\nu_{\rm nfw}$ *missing halos* mostly have an un-relaxed appearance and are probably on-going merger systems. Figures A4 and A5 show two examples of *doubtful peaks* with $\nu_{\rm lens} > 5$. Note that *doubtful peaks* are rare in noise-free κ maps. Most of *doubtful peaks* with $\nu_{\rm lens} > 5$ are associated with substructures of massive halos. Occurrence of the chance projections is very rare, we found three cases with $\nu_{\rm lens} > 5$ in our 30 maps.

[4] http://www.cfht.hawaii.edu/Science/CFHLS/

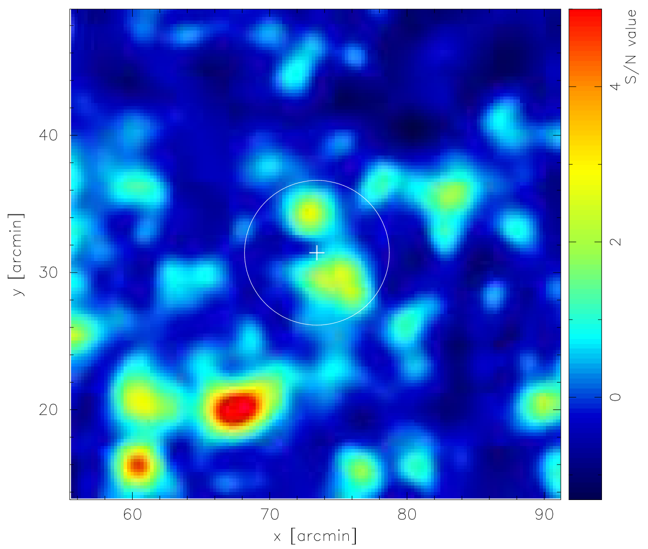

Figure A1. *Missing halo*, an example of a halo with extended matter distribution (possibly in the process of merger). The map apparently shows very eccentric density distribution. The halo has $M_{\rm halo} = 3.4 \times 10^{14} h^{-1} M_\odot$ at $z = 0.37$, and the shape parameters are $Q/Q_{\rm NFW} = 2.1$, $R = 1.4$, and $c/a = 0.23$. The expected peak value is $\nu_{\rm nfw} = 7.0$, but the ν value measured in the lensing map is less than 3.

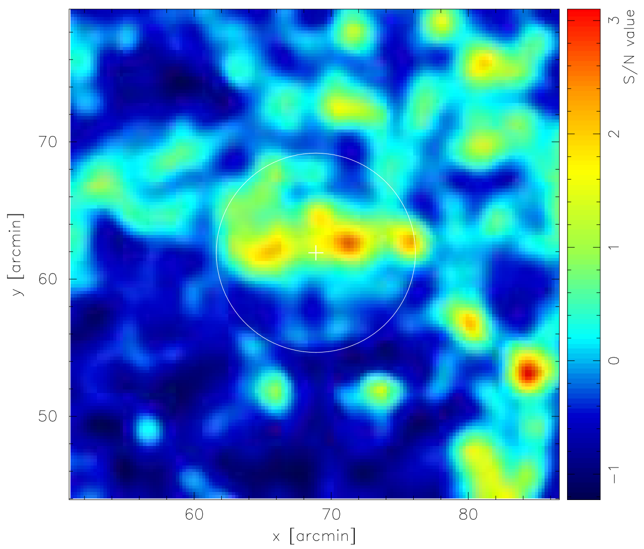

Figure A3. *Missing halo*, an example of an irregular system. The map apparently shows very eccentric density distribution. It is very likely that the halo ($M_{\rm halo} = 1.9 \times 10^{14} h^{-1} M_\odot$, $z = 0.20$ and the shape parameters are $Q/Q_{\rm NFW} = 1.3$, $R = 0.25$, and $c/a = 0.36$.) is a on-going merger system. The expected peak value is $\nu_{\rm nfw} = 6.1$ but the actual ν value is less than 3.

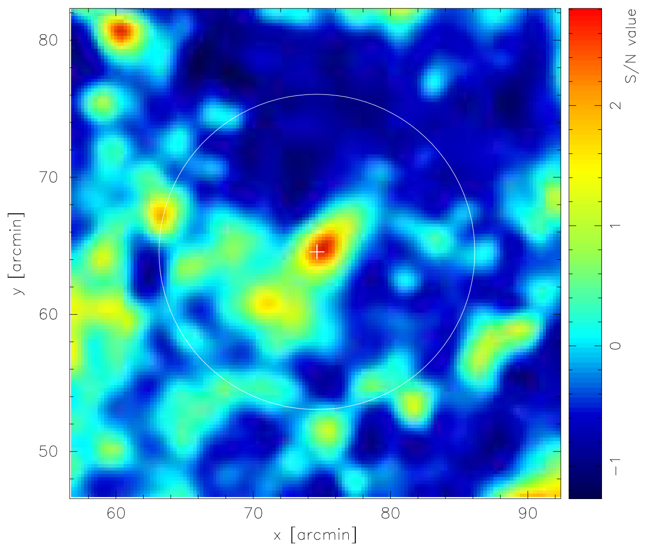

Figure A2. *Missing halo*, an example of low-z un-relaxed system. The plus denotes the center-of-mass position of the halo, and the circle shows the virial radius. The halo ($M_{\rm halo} = 2.0 \times 10^{14} h^{-1} M_\odot$, $z = 0.13$ and the shape parameters are $Q/Q_{\rm NFW} = 1.2$, $R = 0.36$, and $c/a = 0.41$) seems to be not yet reached to a relaxed stage, but probably is a on-going merger system. The expected peak value is $\nu_{\rm nfw} = 6.6$ but the actual ν value is less than 3.

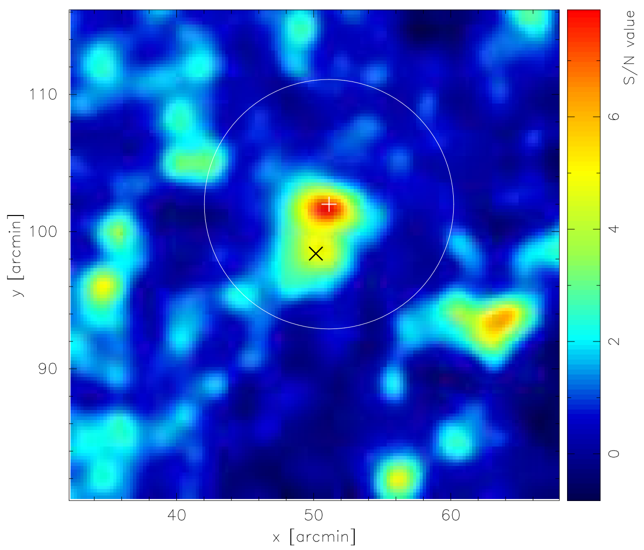

Figure A4. An example of a *local peak* associated with the substructure of a massive halo. The cross denotes the position of the peak with $\nu_{\rm lens} = 5.3$. This is the local peak associated with the substructure of the massive halo ($M_{\rm halo} = 3.5 \times 10^{14} h^{-1} M_\odot$, $z = 0.20$, $\nu_{\rm nfw} = 8.8$ and the shape parameters are $Q/Q_{\rm NFW} = 0.94$, $R = 0.61$, and $c/a = 0.66$). The plus denotes the center-of-mass position of the halo, and the circle shows the virial radius.

APPENDIX B: SIMPLE CORRECTION SCHEME TO THE PEAK COUNTS

As shown in §4 the theoretical model of the peak counts given by eq. (16) underestimates the counts obtained from the realistic noisy κ map by about 20 percent. We here discuss on sources of the change, and develop the correction scheme to the peak counts in an empirical manner. Here we focus on the high peaks of $\nu > 5$.

The sources that modify the peak counts are:

(a) The biased relation between $\nu_{\rm nfw}$-$\nu_{\rm lens}$. In §5.2, it is found that the mean of the differences $\nu_{\rm nfw} - \nu_{\rm lens}$ over class-(i) objects is -0.24. This means that the peak height computed assuming the NFW profile tends to overestimate the real peak height. The reason for this is discussed in §5.2.

(b) Spurious peaks generated by the noise. It is found in the §5

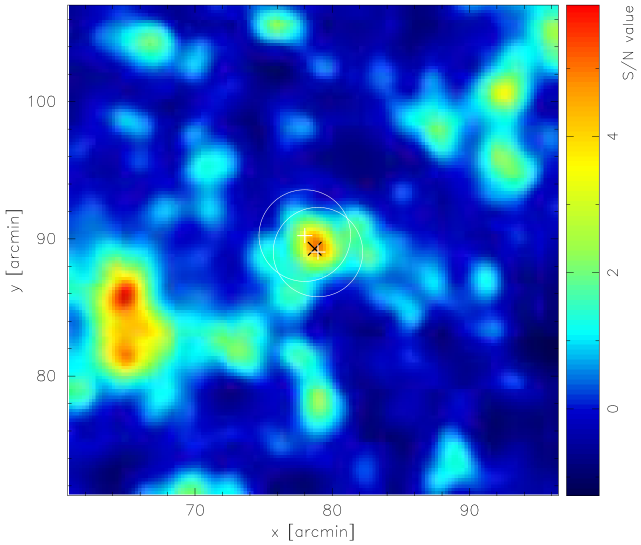

Figure A5. A very rare example of a *chance projection* of two moderately massive halos. The cross denotes the position of the peak with $\nu_{\rm lens} = 5.1$. This peak is not generated by a single halo but generated by the chance projection of three moderately massive halos: ($M_{\rm halo} = 7.5 \times 10^{13} h^{-1} M_\odot$, $z = 0.35$) and ($M_{\rm halo} = 5.4 \times 10^{13} h^{-1} M_\odot$, $z = 0.68$). None of two halos alone can generate the lensing signal larger than $\nu > 3$.

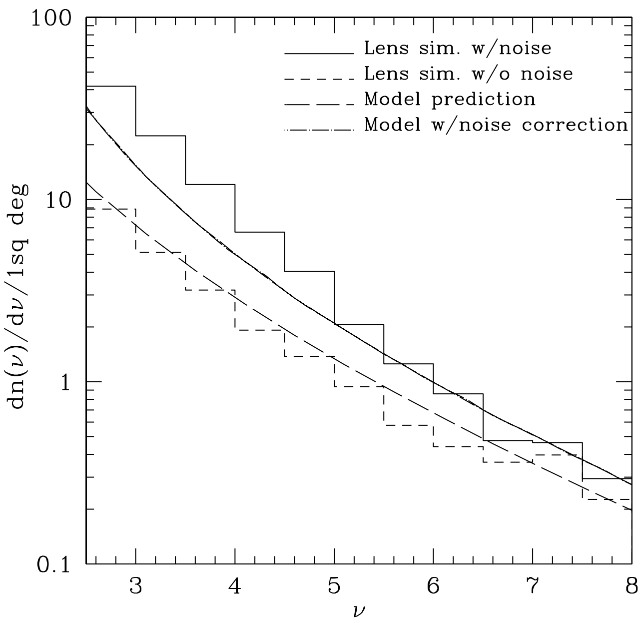

Figure B1. The number count of the lensing peaks per 1 squire degrees. The histograms are from the numerical experiments from the noisy κ maps (solid), and the noise-free κ maps (dashed). The long-dashed line shows the un-corrected model prediction computed from eq. (16), while the sold line shows the corrected model prediction (see text for detail).

that spurious peaks yield about 10% fraction of the total number of high peaks ($\nu > 5$).

(c) The scatter in the relation between $\nu_{\rm noisy}$-$\nu_{\rm lens}$ due to the noise. As will be shown, this scatter increases the peak counts.

(d) The biased relation between $\nu_{\rm noisy}$-$\nu_{\rm lens}$. In §5.3, it is found that the noise produces not only the scatter but also the systematic bias, and that the mean of the differences $\nu_{\rm noisy} - \nu_{\rm lens}$ over class-(i) objects is 0.31. Therefore the peak heights in the noisy κ map are statistically boosted by the noise. The reason for this is discussed in §5.3.

First, we develop the correction scheme for the above point (c). To do this, we take a simplified way, employing the assumption that very high peaks are neither disappeared nor generated by the noise but their peak heights are altered by addition of the noise. In other words, we ignore, for the moment, spurious peaks due to the noise and the other sources. Under the above assumption, the peak counts in the noisy κ map is given by the convolution of the noise free PDF (16) with the Gaussian noise PDF:

$$n_{\rm noisy}(\nu) = \int d\nu' \, \frac{1}{\sqrt{2\pi}} \exp\left(-\frac{\nu'^2}{2}\right) n_{\rm peak}(\nu - \nu'). \qquad \text{(B1)}$$

We further assume that within a small range of ν the peak counts in the original lensing map can be approximated by the exponential form $n_{\rm peak}(\nu) = n_* \exp(p\nu)$, with a constant exponential index of p. As can be seen in Figure B1, this would be a reasonable approximation over a range of $3 \lesssim \nu \lesssim 8$. This approximation allows us to compute the integration in eq. (B1) analytically:

$$\begin{aligned} n_{\rm noisy}(\nu) &\simeq \int d\nu' \, \frac{1}{\sqrt{2\pi}} \exp\left(-\frac{\nu'^2}{2}\right) n_* \exp\left(p(\nu - \nu')\right) \\ &= \exp\left(p^2/2\right) n_{\rm peak}(\nu). \end{aligned} \qquad \text{(B2)}$$

Thus the scatter due to the noise does increase the counts by a factor of $\exp(p^2/2)$.

Turn next to the point (a) and (d) in the above list. From the biases in the relations $\nu_{\rm nfw}$-$\nu_{\rm lens}$ and $\nu_{\rm lens}$-$\nu_{\rm noisy}$ found in the mock data, we derive an approximate mean relation of $\nu_{\rm noisy} - \nu_{\rm lens} = 0.07$. We take this bias by simply shifting the counts as $n_{\rm noisy}(\nu) \to n_{\rm noisy}(\nu + 0.07)$.

Finally, the point (b) is corrected by simply increasing the peak counts by 10 percent.

In Figure B1, the corrected model prediction is plotted and is compared with the results from numerical experiments. To compute the corrected model prediction, $n_{\rm noisy}(\nu)$, we first computed the uncorrected counts $n_{\rm peak}(\nu)$ at a small interval of $\delta\nu$ using eq. (16). Then the local exponential slope of the counts is evaluated by a finite differential scheme $p(\nu_i) = [\log n(\nu_{i+1}) - \log n(\nu_i)]/\delta\nu$. We compute $n_{\rm noisy}(\nu)$ using the eq. (B2) with this $p(\nu_i)$. Then, the correction $n_{\rm noisy}(\nu) \to n_{\rm noisy}(\nu + 0.07)$ was made for $p(\nu_i)$ at every ν_i to correct the points (a) and (d). Finally the counts is increased by 10 percent to correct the point (b). The corrected prediction agrees with the noisy counts reasonably well at least $\nu > 5$, where the above approximations are valid. On lower peak heights $\nu < 4$, the prediction is systematically smaller than the measurement, where false peaks due to the noise have larger contribution. Note that the amplitude of the effects (b) and (d) may depend on the noise properties and on the choice of the smoothing scheme.

It is clearly seen in the Figure B1 that the corrected peak counts has a slope very similar to the un-corrected counts. Therefore, one may simply make a correction to the model prediction obtained from eq. (16) by simply multiplying the factor 1.2, which gives an alternative approximate way to compute the corrected peak counts.

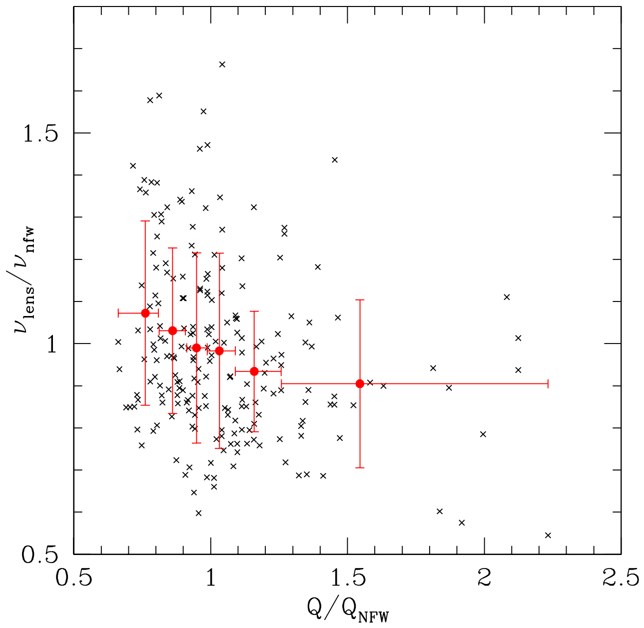

Figure C1. The scatter plot showing the distribution of the halos in $Q/Q_{\rm NFW}$–$\nu_{\rm lens}/\nu_{\rm nfw}$ plane. The class-(i) halos having $\nu_{\rm nfw} > 4$ and $\nu_{\rm nfw} > 4$ only are plotted. The filled circles show the average over 35 halos within bins whose ranges are denoted by the x-error bars, while the y-error bars denote RMS among the halos.

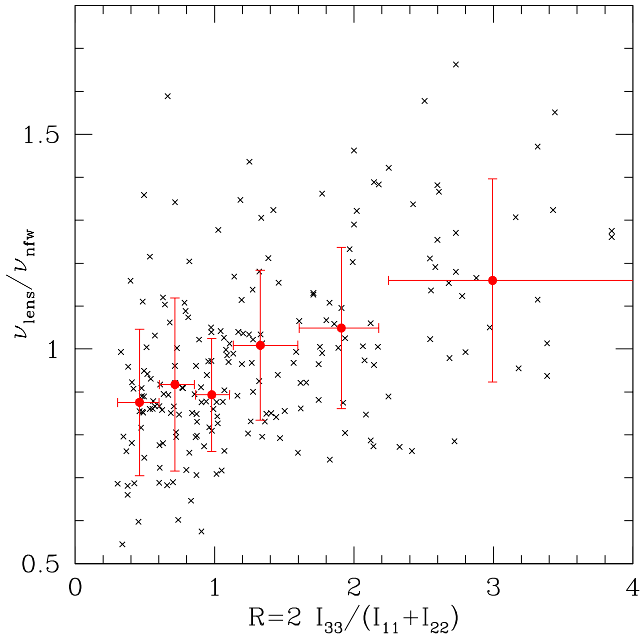

Figure C2. Same as Figure C1 but for R–$\nu_{\rm lens}/\nu_{\rm nfw}$ plane.

APPENDIX C: RELATIONS BETWEEN THE HALO SHAPE AND κ AMPLITUDE

Here we examine the effect of the individuality in the halo mass distribution on the amplitude of the κ peak. Figures C1 and C2 show how the ratio $\nu_{\rm lens}/\nu_{\rm nfw}$ varies with the halo shape parameters Q and R (see equations (19) and (22) for the definitions), where we consider the class-(i) halos with $\nu_{\rm nfw} > 4$ and $\nu_{\rm lens} > 4$ only. The filled circles show the average over halos sitting in the range denoted by the x-direction bar, where each interval is defined so that it contains 35 halos, and the error bar in y-direction denotes the RMS among them.

The correlations between the shape parameters and amplitude of the lensing signal are observed in both the figures, though the statistical significance is not very high. The unti-correlation in the $\nu_{\rm lens} - Q$ is because more concentrated mass distribution ($Q < 1$) compared to the average NFW profile provides greater lensing signal. The lensing signal is also amplified if mass distribution within a halo is elongated along the line-of-sight ($R > 1$). However, we draw attention to the rather large scatters in these relations that may arise from the following two sources. First, the shape parameters we employ characterize rather global mass distribution within a halo and cannot describe the detailed structures. Second, probably more important one is the projection effect due to different structures along the same line-of-sight of the halo.